CHALMERS

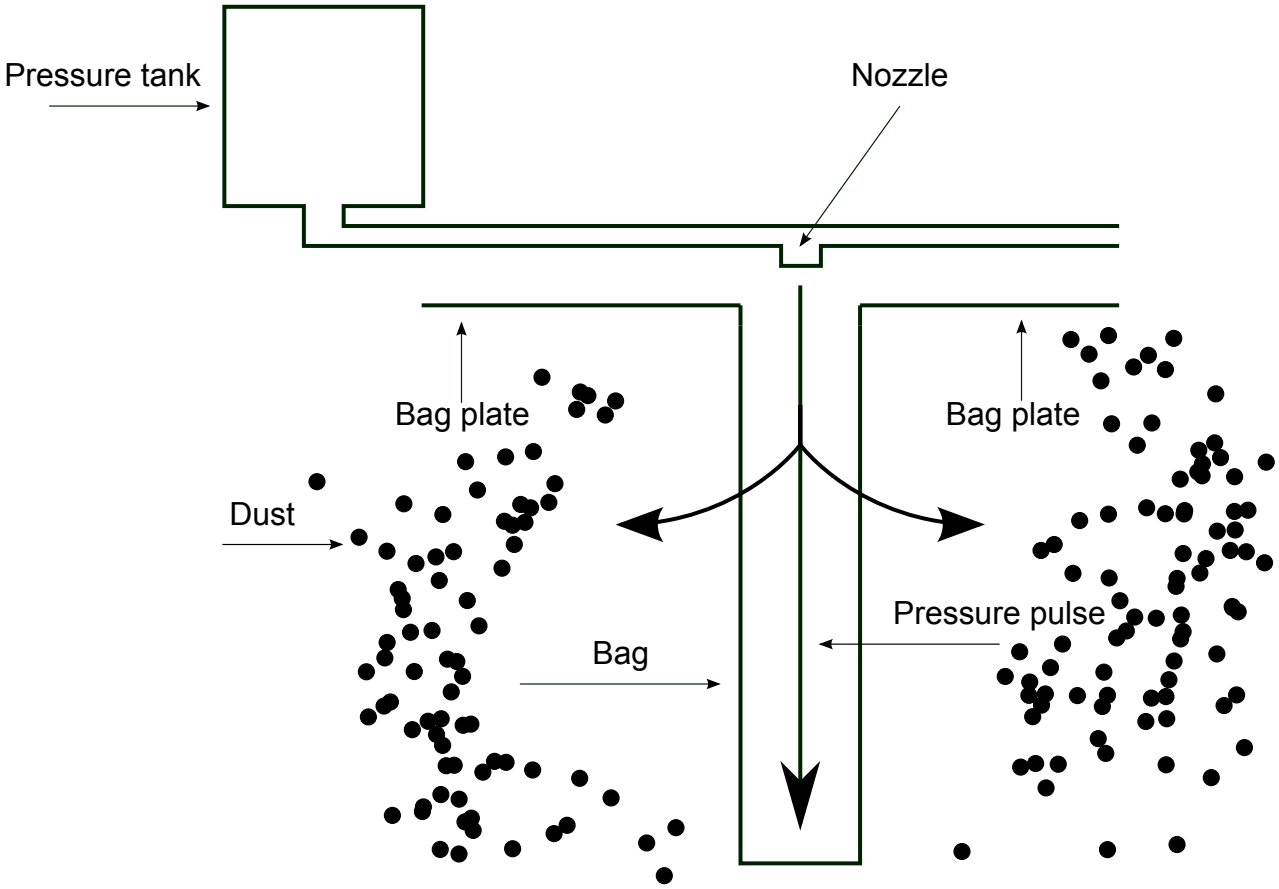

Arbitrary Lagrangian-Eulerian Simulations of a Pressure Pulse inside a Flexible Porous Fabric Bag

Master's thesis in Applied Mechanics

DENNIS CARLSSON

Department of Applied Mechanics
Division of Dynamics
CHALMERS UNIVERSITY OF TECHNOLOGY
Göteborg, Sweden 2014
Master's thesis 2014:41

MASTER'S THESIS IN APPLIED MECHANICS

Arbitrary Lagrangian-Eulerian Simulations of a Pressure Pulse inside a Flexible Porous Fabric Bag

DENNIS CARLSSON

Department of Applied Mechanics
Division of Dynamics
CHALMERS UNIVERSITY OF TECHNOLOGY
Göteborg, Sweden 2014

Arbitrary Lagrangian-Eulerian Simulations of a Pressure Pulse inside a Flexible Porous Fabric Bag
DENNIS CARLSSON

Master's thesis 2014:41
ISSN 1652-8557
Department of Applied Mechanics
Division of Dynamics
Chalmers University of Technology
SE-412 96 Göteborg
Sweden
Telephone: +46 (0)31-772 1000

Cover:
A pressure pulse is injected inside a fabric bag to remove dust from the bag surface

Chalmers Reproservice
Göteborg, Sweden 2014

Arbitrary Lagrangian-Eulerian Simulations of a Pressure Pulse inside a Flexible Porous Fabric Bag
Master's thesis in Applied Mechanics
DENNIS CARLSSON
Department of Applied Mechanics
Division of Dynamics
Chalmers University of Technology

Abstract

In today's society, combustion processes are important for heat and power generation. A negative effect of the combustion processes are the increase of emissions in the air which can affect the environment and human health in a negative manner. To reduce emissions and increase air quality, Air Quality Control Systems (AQCS) can be used. There are different kinds of AQCS but in this thesis the focus is on fabric filters, which is an AQCS that reduce the amount of particles and dust in the air. In a fabric filter there are hundreds of fabric bags, hanging in the ceiling of the filter. The air is flowing through the bag and the dust gets stuck on the surface of the bag. When the bag gets covered by dust, the filtering effect decrease and the bag needs to be cleaned. The cleaning of a bag is done by a powerful pressure pulse on the inside of the bag. The pressure pulse gives the bag an acceleration, which removes the dust from the bag. In this thesis a parameter study was made to see how the acceleration was affected by different parameters. The considered parameters were the permeability of the bag and the weight of the dust on the bag surface and these were compared to a reference case representing a clean bag. There existed experimental results that were compared to the simulation results.

The cleaning of a bag was modelled in LS-DYNA using the Arbitrary Lagrangian-Eulerian (ALE) approach with a fluid-structure interaction between the bag and the air. Unfortunately, the pressure propagated much slower in the simulations compared to the experiments and also the magnitude of the pressure pulse was to low. The reason for this was probably due to the boundary condition defining the pressure pulse. Even if the pressure was not accurate in all respects, the acceleration of the bag was investigated to see if any trends of how the bag was affected by the different parameters could be found. Unfortunately, an uneven distribution of initial deformation (also called slack), made it hard to predict some aspects regarding the acceleration due to that the acceleration differed a lot between different points at the same height on the bag. To be able to use this kind of simulations to improve the cleaning of a bag, the pressure pulse needs to be defined in such a way so that it get a better agreement with the experimental result. Also a method about how the accelerations should be measured needs to be investigated.

Keywords: Arbitrary Lagrangian-Eulerian, ALE, Fluid-Structure Interaction, FSI, Fabrics, Porous

Preface

In this study, the possibilities to model the dynamics of a fabric bag resulting from a pressure pulse during cleaning were investigated. The thesis was made during January to June 2014 at ALSTOM POWER SWEDEN AB in Växjö. I want to thank my supervisor at ALSTOM, Micko Björck, for his dedication and help during this thesis. I also want to thank Robert Moestam and Lars-Erik Johansson at the ALSTOM laboratory for providing me with experimental data and tips about the modelling approach. Also a thank to Matthias Kirchhoff at BWF Envirotec in Offingen, Germany for providing me with material data for the fabric bag. A special thanks to Livermore Software Technology Corporation (LSTC) in Livermore, CA, United States for providing me with free licenses to the finite element program LS-DYNA, which have been used in this thesis. I also want to thank my examiner at the department of Applied Mechanics, division of Dynamics at Chalmers Univeristy of Technology, Peter Folkow, for support during the thesis. Also a thank to Karin Brolin for help with LS-DYNA related questions.

Växjö, June 2014
Dennis Carlsson

Nomenclature

Roman Symbols

Symbol	Description
A_n	Ergun's viscous coefficient
B_n	Ergun's inertial coefficient
C_p	Specific heat at constant pressure
C_v	Specific heat at constant volume
d	Penetrating distance
D_{ijkl}	Stiffness tensor
e	Total internal energy per unit mass
E_{ij}	Green-Lagrange strain tensor
F_i	Force vector
F_{ij}	Deformation gradient
e_0	Total initial energy per unit mass
I_0	Momentum
$\bar{I}_{ij}$	Moment of inertia tensor
k_s	Contact stiffness
$\bar{L}_i$	Angular momentum vector around center of gravity
m	Mass
$\bar{M}_i$	Moment vector around center of gravity
n_i	Normal vector
p	Pressure
p_0	Total pressure
R	Gas constant
t	Time or thickness
Δt_{cr}	Critical time step size
T	Temperature
u_i	Displacement vector
v_i	Velocity vector
$\hat{v}_i$	Mesh velocity vector
v_n	Relative velocity
W	Energy/Work
x_i	Spatial coordinate vector
X_j	Reference position vector

Greek Symbols

Symbol	Description
γ	Ratio of the specific heats
δ_{ij}	Kronecker's delta function
ε	Porosity
ε'_{ij}	Strain rate tensor
μ	Dynamic viscosity
ρ	Density
σ_{ij}	Cauchy stress tensor
σ'_{ij}	Deviatoric Cauchy stress tensor
ϕ	Transport quantity
$\bar{\omega}_i$	Angular velocity vector
$\omega_{\max}$	Highest eigenfrequency

Abbreviations

ALE	Arbitrary Lagrangian-Eulerian
AQCS	Air Quality Control Systems
FEM	Finite Element Method
FSI	Fluid Structure Interaction
LSTC	Livermore Software Technology Corporation
MMALE	Multi Material Arbitrary Lagrangian-Eulerian

Contents

1 Introduction

In today's society, combustion processes are of great industrial interest. Different applications may be pulp & paper, transforming waste to energy and heat & power generation where e.g coal, oil, biomass are used as fuel [1]. The combustion processes lead to an increase of emissions in the air which may impact human health and the environment in a negative manner [11]. To reduce emissions and to improve air quality, Air Quality Control Systems (AQCS) can be used. There are various AQCS which reduce different types of emissions, e.g NO_x, SO_2, mercury, particles. An integrated emission control plant containing several of these systems can be seen in Figure 1.1. This thesis will only consider control systems for particle reduction, specifically fabric filters.

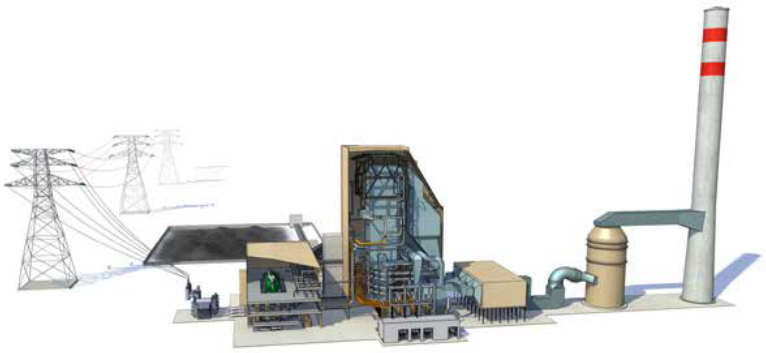

Figure 1.1: *A complete Emission Control System (ECS) park from ALSTOM [1]*

A fabric filter can be seen in Figure 1.2 where air containing dust and particles (raw gas) is flowing into the filter and leaving as clean air. Inside the fabric filter hundreds of fabric bags are hanging in a bag plate located

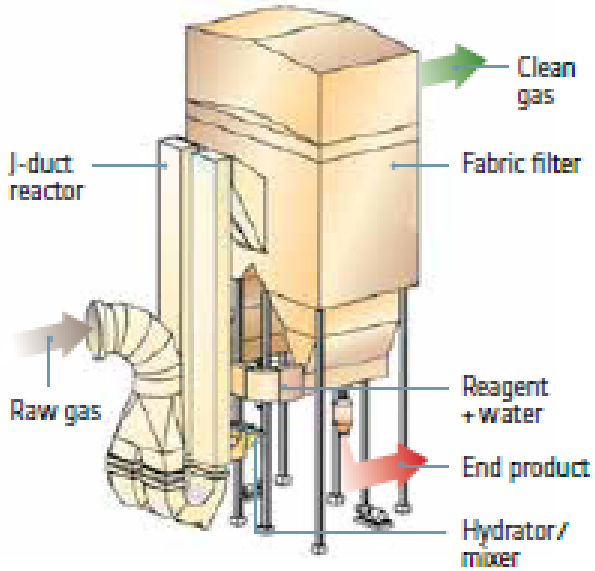

Figure 1.2: *A fabric filter where raw gas air enters the filter and leaves as clean air [2]*

near the ceiling of the fabric filter. As the air is flowing through the bags, the dust particles get stuck on the surface of the bags meanwhile the air continues its journey through the filter as can be seen in Figure 1.3. The

bag itself can be seen in Figure 1.4 and in Figure 1.5 where the bag is spanned by a bag cage to maintain the shape and filtering area of the bag. Without the bag cage the bag would crumple up and the filtering effect would decrease significantly. After a while the bags become totally covered with dust and a thin dust

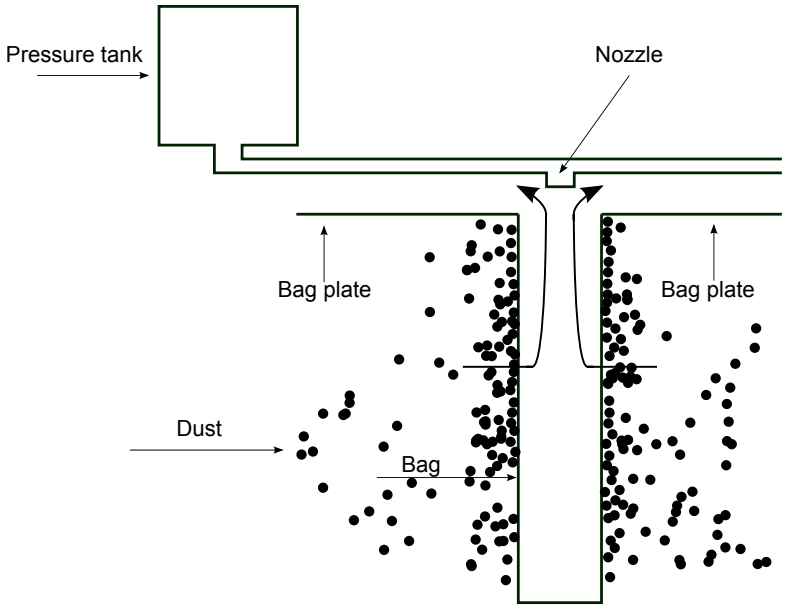

Figure 1.3: *Air with dust is flowing inside a fabric filter. The dust get stuck on the surface of the bag meanwhile the clean air continues through the filter.*

Figure 1.4: *A fabric bag that is used in a fabric filter*

cake takes form on the bag surface. The dust cake reduces the filtering effect through the bags. The cleaning of a bag is done by a powerful pressure pulse that expands the bag and gives the bag an acceleration. This acceleration together with the flow from the pressure pulse pushes the particles away from the surface of the bag. This is illustrated in Figure 1.6. With the length of the bags that is used today the cleaning process works well, but to improve the cleaning and hence be able to increase the length of the bag ALSTOM wants to understand how the acceleration is affected by different parameters. This is not well studied yet even if some experiments have been done. This kind of problem can be studied through computer simulations with a model that considers the physics involved.

Figure 1.5: *A bag cage that force the bag to maintain its cylindrical shape*

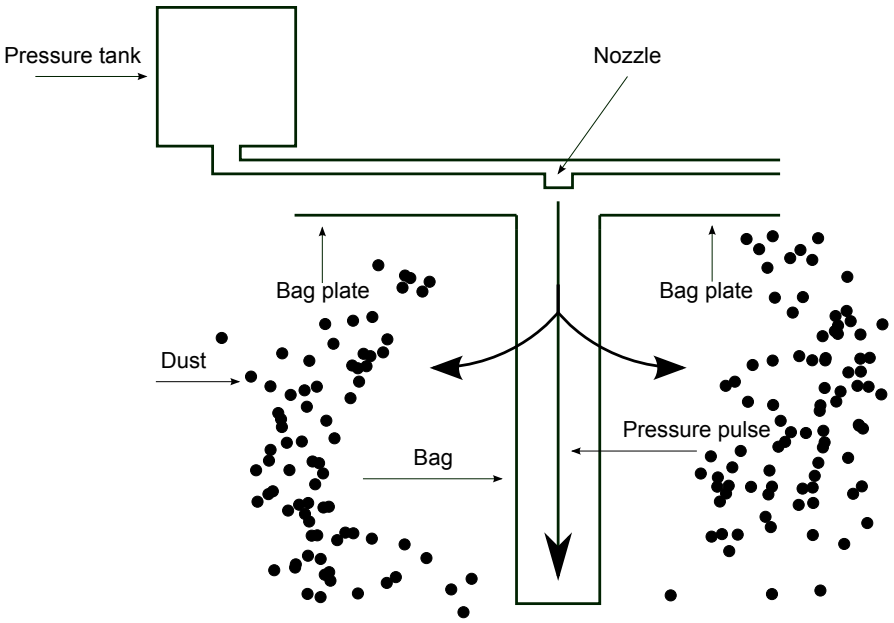

Figure 1.6: *To clean a bag high pressure air is shot into the bag through the nozzle*

1.1 Background

It does not exist much information about the behaviour of the fabric bag in a fabric filter. A lot of complex physical aspects must be considered. The bag is made of a highly flexible porous fabric material with high degree of anisotropy and non-linear properties [14]. The flow interaction is very complex due to that the flow may deform the bag, which on the other hand will change the flow behaviour, i.e there may be a two way coupling between the flow and the structure. Also, simultaneously, air flows through the porous fabric material. The flow through the fabric is important to consider in many applications. Even if there are few public studies done on flow interaction with bags in a fabric filter other applications may be useful when studying the behaviour of the fabric bag. For example both airbags and parachutes handle flows through a porous deforming fabric material. For both airbags and parachutes it is possible to model the Fluid-Structure Interaction (FSI) using different Finite Element based programs. In [22] an airbag deployment is simulated using Coupled Eulerian-Lagrangian (CEL) in Abaqus/Explicit. The result from the simulation shows similarities with experiments which concludes that this approach suits well for airbags. In that simulation the air on the outside is not considered due to that it is assumed that the inflator pressure inside the airbag is much higher than the surrounding air pressure. It is a common assumption for airbag designers to only consider the air remaining inside the airbag [25]. Also [15] consider an airbag deployment but in the software LS-DYNA. Unfortunately, neither [22] nor [15] uses real porosity or permeability properties in the simulations which means that the leakage from the airbag is

modelled as a uniform massflow leakage or a damping coefficient [21, 25]. The reason why this is not defined in [22] is because porosity is not supported in the Abaqus/Explicit but only in Abaqus/Standard [21] and for [15] porosity was not supported in LS-DYNA at that time. In a paper of Benjamin Tutt [25], he points out the importance of considering the influence from the air even after it passes through a parachute fabric. The paper describes parachute simulations with and without permeability and these results are compared with experimental data. The compared parameter is the drag coefficient, C_D, which is a crucial parameter for the parachute designer. The simulation considering permeability predicts 1.6 % lower C_D than the experiment and the simulation without consideration to permeability predicts 25 % higher C_D than the experiment. The results from the paper validate the permeability algorithm in LS-DYNA and show that the permeability may have a great impact on the result. Some other papers considering similar parachute simulations are [24, 26, 27, 29].

1.2 Purpose and problem description

The purpose with this thesis is to model the cleaning of a dust covered bag. A parameter study is done and the bag dynamics (acceleration, deformation etc) are evaluated. A reference case representing a clean bag at standard conditions will be used to compare the results from the simulations. This reference case is compared to experimental results to see if the modelling approach works. The simulations are performed in the Finite Element based software LS-DYNA from Livermore Software Technology Corporation (LSTC) which is used in other applications considering flows through porous flexible materials.

1.3 Delimitations

In a fabric filter there are hundreds of bags. All these bags will not be modelled due to that it will be to computational demanding. Therefore the model will only consist of one bag. Also, the fabric material will not be modelled at micro level, but the effects from the micro structure will be modelled at a macro level using Young's modulus. Also there are some limitations in the FE code due to some simplifications. Most of the simplifications are made in the fluid modelling and those limitations are mentioned more in the modelling set-up of this thesis.

2 Theory

This chapter gives an introduction to the theory used in this thesis. The theory presented here is in some cases simplified and shows just the principles that is necessary to understand the thesis.

2.1 Arbitrary Lagrangian-Eulerian simulations

Arbitrary Lagrangian-Eulerian (ALE) simulations is a great method to use when there is a strong coupling between a fluid and a structure. A great part of this section is based on [4, 9] and requires some basic knowledge in the Finite Element Method (FEM) which will not be considered here. Instead [20] is recommended as reading material for those unfamiliar with FEM.

2.1.1 Lagrangian and Eulerian formulation

In computer codes there are different kinematic algorithms to determine the relation between the deforming continuum and the finite mesh. Two classical algorithm descriptions are the Lagrangian and Eulerian description. In the Lagrangian description each node of a finite mesh is deformed together with the continuum material. The advantage of this is that the Lagrangian description tracks the surface of the continuum material, i.e the shape of the deforming material can be determined. A drawback of this description is that it is inaccurate when there are large distortions of the mesh which easily appears with large deformations. The Lagrangian description is often used for structural analysis. The Eulerian description uses a mesh that is fixed in space. The advantage of the Eulerian description is that it handles large distortions, but uses a description that is fixed in space complicates the surface tracking. Also advection over element boundaries must be considered. The Eulerian description is often used in fluid dynamics where large deformations often occur. A developed method that combines the advantages of both descriptions is the ALE method. In this method the nodes of the mesh can be moved as in the Lagrangian description or be held as in the Eulerian description. Also, the nodes can move without following the continuum material and this is done to minimize the advection over the boundaries to get a more accurate solution.

2.1.2 Multi Material Arbitrary Lagrangian-Eulerian description

The Multi Material Arbitrary Lagrangian Eulerian (MMALE) description is based on three domains: the initial material configuration, the current (deformed) material configuration and the ALE configuration, also called reference configuration. The initial and current configurations determine together the motion of the material. The current configuration also, together with the ALE configuration, determine the mesh motion [4]. If the mesh motion is zero, the mesh is considered to be an Eulerian mesh. The only thing that differs MMALE from ALE is that the MMALE handles multiple materials in the same element, even if the number of materials simultaneously appearing in the same element is limited to at most 3 [16]. In the elements of the mesh, the governing equations for mass, momentum and energy are centred integrated while other variables are stored in the nodes. The governing equations are written in index notation (see Appendix A) as [4, 8, 9]

$$\frac{\partial \rho}{\partial t} + \rho \frac{\partial v_i}{\partial x_i} + (v_i - \hat{v}_i)\frac{\partial \rho}{\partial x_i} = 0 \tag{2.1}$$

$$\rho \frac{\partial v_i}{\partial t} + \rho (v_i - \hat{v}_i)\frac{\partial v_j}{\partial x_j} = \frac{\partial \sigma_{ij}}{\partial x_j} + \rho f_i \tag{2.2}$$

$$\rho \frac{\partial e}{\partial t} + \rho (v_i - \hat{v}_i)\frac{\partial e}{\partial x_i} = \sigma_{ij}\frac{\partial v_i}{\partial x_j} \tag{2.3}$$

where the time derivatives on the left hand side are expressed in the reference configuration (ALE configuration) and the right hand side is expressed in the current material coordinates. Here ρ is the density, v_i is the material velocity, $\hat{v}_i$ is the mesh velocity or the reference velocity, σ_{ij} is the Cauchy stress tensor, f_i is the body density force and e denotes the total internal energy per unit mass. Setting $\hat{v}_i = v_i$ gives the Lagrangian description of the equations while $\hat{v}_i = 0$ gives the Eulerian description. The stress tensor σ_{ij} can be split into an isotropic and a deviatoric part [6, 10]

$$\sigma_{ij} = \frac{1}{3}\sigma_{kk}\delta_{ij} + \sigma'_{ij} \tag{2.4}$$

where δ_{ij} is the Kroneckers delta function which equals unity if $i = j$ and equals zero if $i \neq j$. This means that the first term in eq (2.4) is only active in the normal directions. As pressure p acts in negative normal direction we conclude that $\sigma_{kk}/3 = -p$ in eq (2.4) [6]. The deviatoric part σ'_{ij} contains the shear stress and is defined as [17]

$$\sigma'_{ij} = 2\mu\varepsilon'_{ij} \tag{2.5}$$

where μ is the dynamic viscosity and ε'_{ij} is the strain rate tensor defined as

$$\varepsilon'_{ij} = \frac{1}{2}\left(\frac{\partial v_i}{\partial x_j} + \frac{\partial v_j}{\partial x_i}\right) \tag{2.6}$$

Inserting all together, a final expression for the stress tensor is achieved

$$\sigma_{ij} = -p\delta_{ij} + \mu\left(\frac{\partial v_i}{\partial x_j} + \frac{\partial v_j}{\partial x_i}\right) \tag{2.7}$$

In the one dimensional case of the governing equations there are four unknown variables, ρ, $v_{i=1}$, e and p but there are only three equations. Therefore an extra equation is needed to close the system. The required equation is the equation of state which determine the pressure. The equation of state is dependent on the problem type but for a gas the ideal gas law can be used

$$p = \rho RT = \rho(C_p - C_v)T \tag{2.8}$$

where ρ is the density, T is the temperature, C_p and C_v are the specific heat coefficients at constant pressure and constant volume, respectively. Using the ideal gas approach the initial energy per unit mass for the fluid is defined as $e_0 = C_v T$ where the total initial energy per unit mass is defined as $e = e_0 + (1/2)v_i v_i$. In the three dimensional case there are three velocity components v_i, where $i = 1, 2, 3$ but there are also two extra equations for the momentum and together with the equation of state the system will be closed.

When solving the ALE formulation, LS-DYNA first calculates a Lagrangian cycle where the mesh follows the material. The cycle after that is called the advection cycle and during this cycle the mesh is arbitrary moved to a new position or moved back to its initial position. If the mesh is an Euler mesh it will always go back to its initial position but if the mesh is an ALE mesh it can go to an arbitrary position that is more suitable than the Lagrangian and Eulerian positions. This is illustrated in Figure 2.1.

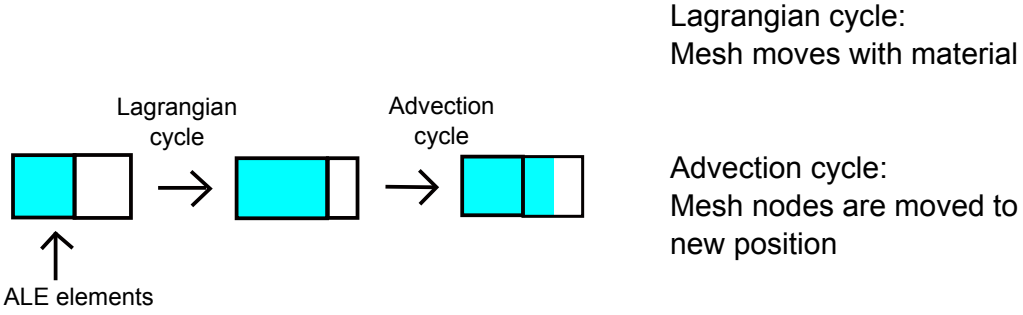

Figure 2.1: *The ALE mesh (black boundaries) first moves with the material (blue in the figure) in the Lagrangian cycle and later moves to a more suitable position in the advection cycle*

2.2 Solid bodies

When describing the motion and deformation of a solid body three main governing equations are used; conservation of mass, conservation of momentum and conservation of angular momentum

$$\frac{\partial \rho}{\partial t} + \rho\frac{\partial v_j}{\partial x_j} = 0 \tag{2.9}$$

$$\rho\frac{\partial v_i}{\partial t} = \frac{\partial \sigma_{ij}}{\partial x_j} + \rho f_i \tag{2.10}$$

$$\bar{M}_i = \dot{\bar{L}}_i \quad \text{where} \quad \bar{L}_i = \bar{I}_{ij}\bar{\omega}_j \tag{2.11}$$

Equation (2.9) and (2.10) are the same as (2.1) and (2.2) in the ALE section but with the Lagrangian formulation instead. In eq (2.11) $\bar{L}_i$ is the angular momentum, $\bar{I}_{ij}$ the moment of inertia, $\bar{\omega}_j$ angular velocity and $\bar{M}_i$ the moment [5]. A bar over a notation means that it is considered around the center of mass and a dot over a notation indicates time derivative. The conservation of angular momentum is used to prove symmetry of the stress tensor, $\sigma_{ij} = \sigma_{ji}$. The proof can be seen in Appendix B. This reduce the unknowns of σ_{ij} from nine to six components. Still there are more unknowns than equations and therefore the generalized Hooke's law is used to express the stresses

$$\sigma_{ij} = D_{ijkl}E_{kl} \tag{2.12}$$

Here D_{ijkl} is a forth order stiffness tensor and E_{kl} is the Green-Lagrange strain tensor which is used when large deformations are present [23]. The Green-Lagrange strain tensor is defined by the deformation gradient F_{ij}

$$E_{ij} = \frac{1}{2}(F_{ki}F_{kj} - \delta_{ij}) \tag{2.13}$$

$$F_{ij} = \frac{\partial x_i}{\partial X_j} \tag{2.14}$$

where x_i is the current position and X_j is the reference (undeformed) position. The displacement can be expressed as

$$u_i = x_i - X_i \tag{2.15}$$

Equation (2.14) and (2.15) into (2.13) gives a final expression for the Green-Lagrange strain as

$$E_{ij} = \frac{1}{2}\left(\frac{\partial u_i}{\partial X_j} + \frac{\partial u_j}{\partial X_i} + \frac{\partial u_k}{\partial X_i}\frac{\partial u_k}{\partial X_j}\right) \tag{2.16}$$

If the body have small deformations the last term in eq (2.16) will be very small and the deformed and the undeformed reference location will almost coincide

$$E_{ij} = \frac{1}{2}\left(\frac{\partial u_i}{\partial X_j} + \frac{\partial u_j}{\partial X_i}\right) \approx \frac{1}{2}\left(\frac{\partial u_i}{\partial x_j} + \frac{\partial u_j}{\partial x_i}\right) = \varepsilon_{ij} \tag{2.17}$$

which means that for small deformations the Green-Lagrange strain can be approximated by the engineering strain ε_{ij}.

2.3 Fluid-structure interaction

In many applications it is suitable to treat parts in different formulations. For example in fluid structure interaction it is often a good choice to treat the fluid in Eulerian or ALE-formulation and the structure in Lagrangian formulation. Therefore a coupling algorithm is needed for the different parts to communicate [19]. For this coupling to work properly it is required that at least 2 or 3 coupling points per ALE element length are used during the whole simulation. These coupling points should be defined with care. In LS-DYNA these points are defined on the Lagrangian segments which means that the user must consider the relative mesh size between the Lagrangian and ALE mesh at the location of contact. Also too many coupling points may lead to instabilities and too few lead to leakage [16]. Two methods for the coupling in LS-DYNA are the constrained based and the penalty based coupling. Both methods require that the ALE (or Eulerian) and the Lagrangian mesh overlap even if the nodes do not need to coincide [13].

2.3.1 Constrained based coupling

In the constrained based approach the ALE nodes that get in contact with Lagrangian structures are projected to the structure and are forced to follow the movement of the structure [13, 19]. This approach conserves momentum but does not conserve energy. To show this, consider an ALE particle with mass m and velocity v_0 impacting with a non-moving structure with mass m, as seen in Figure 2.2. Before impact the momentum I_0 and energy W_0 are

$$I_0 = mv_0 \tag{2.18}$$

$$W_0 = \frac{1}{2}mv_0^2 \tag{2.19}$$

When the ALE particle impacts the Lagrangian structure it get stuck on the Lagrangian structure. The momentum is conserved during the impact which gives a velocity $v_1 = \frac{1}{2}v_0$ for the system after the impact which can be concluded from eq (2.20). As a result of this new velocity the kinetic energy after the impact is lower than before the impact which can be seen in eq (2.21).

$$I_1 = (m+m)v_1 = 2mv_1 = I_0 \tag{2.20}$$

$$W_1 = \frac{1}{2}(2m)(v_1)^2 = \frac{1}{2}(2m)\left(\frac{1}{2}v_0\right)^2 = \frac{1}{4}mv_0^2 < W_0 \tag{2.21}$$

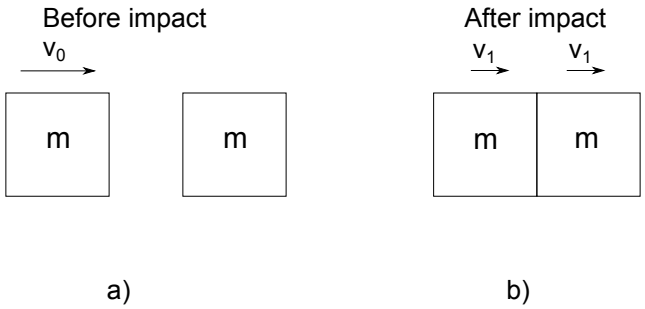

Figure 2.2: *a) An ALE particle (left) is travelling ahead a non moving structure (right) b) After impacting the structure, the ALE particle is moving together with the structure at the same speed*

2.3.2 Penalty based coupling

In the penalty based approach coupling forces are added to both ALE and Lagrangian elements if the Lagrangian part is penetrating the ALE material. The magnitude of this force is proportional to the penetrating distance. The position of a coupling point at a time t_1 is compared to the location at time t_0 and from this the penetration distance can be measured. This can be seen in Figure 2.3. The applied force is

$$F_i = k_s d n_i \tag{2.22}$$

where k_s is the contact stiffness defined by the material properties, d is the penetration distance and n_i is the unit normal vector at the contact point on the Lagrangian part. The penalty based coupling conserves both momentum and energy but are not as stable as the constrained based one [19].

2.4 Advection algorithms

When preforming ALE simulations the use of an advection algorithm is needed to approximate the centered stored variables like density, the stress tensor, internal energy and history variables at the element face due to relative motion between the material and the ALE mesh [13]. A good advection algorithm should be monotonic, conservative and as little dissipative and dispersive as possible [19]. That means that the advection algorithm should not introduce new maximum or minimum values (monotonic) and should not change the total mass, momentum etc of the system (conservative). A dissipative scheme smears out the variable fields and a dispersive scheme make high spatial frequencies in the solution variable field travel slower than the mass flow velocity [13, 19]. In LS-DYNA there are two different algorithms (with some different versions of those), the Donor Cell algorithm and the Van Leer scheme [18].

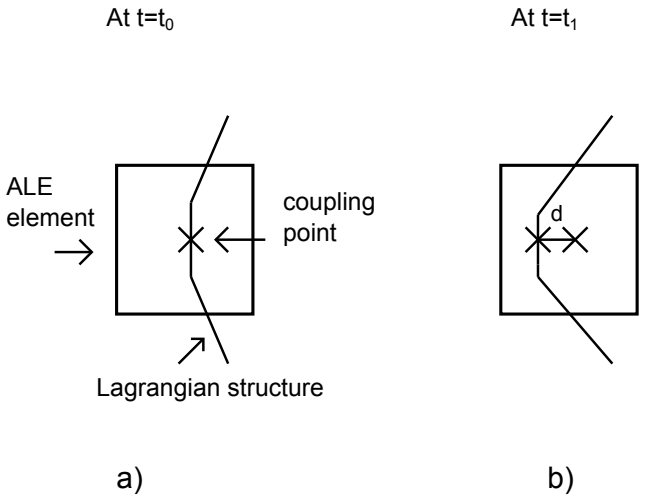

Figure 2.3: *a) Lagrangian structure penetrates an ALE element and the position of the coupling point at time t_0 is registered b) At time t_1 the penetrating distance d can be measured from the updated position of the coupling point*

2.4.1 Donor Cell algorithm

The Donor Cell Algorithm is a first order algorithm that is stable, monotonic and fast but it is also strongly dissipative and dispersive. However, due to the strong dissipation, the high frequencies that travel to slow are quickly damped out [19]. This limits the use of the Donor cell algorithm to fluids [19]. The one dimensional Donor Cell Algorithm for a transport quantity, ϕ, between node j and $j+1$, is

$$\begin{aligned} \phi_{j+1/2}^{n+1} &= \phi_{j+1/2}^{n} + \frac{\Delta t}{\Delta x}(f_j^\phi - f_{j+1}^\phi) \\ f_j^\phi &= \frac{a_j}{2}(\phi_{j-1/2}^n + \phi_{j+1/2}^n) + \frac{|a_j|}{2}(\phi_{j-1/2}^n - \phi_{j+1/2}^n) \end{aligned} \tag{2.23}$$

where $\phi_{j-1/2}^n$ and $\phi_{j+1/2}^n$ are the initial values of ϕ to the left and right of node j, respectively. a_j is the velocity at node j which also decides the sign of f_j^ϕ and thereby also the upstream direction [18].

2.4.2 Van Leer MUSCL scheme

The Van Leer MUSCL Scheme is a scheme that is monotonic, conservative and second order accurate. This scheme is much slower than the Donor cell algorithm [19]. The principles of the Van Leer scheme is to include a linear variation of the field variable ϕ over an element. This is done by introducing a piecewise linear function, ϕ_L. The slope, S, of this piecewise linear function over an element in one dimension can be calculated by using central differencing

$$S_i = \frac{\phi_{i+1} - \phi_{i-1}}{L} \tag{2.24}$$

where i indicates the element. Using only the central differencing to calculate the slope over an element may introduce new minimum and maximum values as seen in Figure 2.4 and therefore another formulation is needed to ensure a monotonic scheme. In this new formulation the maximum allowed slope at the left and to the right of an element are calculated. How these slopes are defined can be seen in Figure 2.5 together with the slope from the usage of central differencing. The maximum slope to the left, s^L, and to the right, s^R, are expressed as

$$\begin{aligned} s^L &= \frac{\phi_i - \phi_{i-1}}{L^-} \\ s^R &= \frac{\phi_{i+1} - \phi_i}{L^+} \end{aligned} \tag{2.25}$$

Now when the maximum slopes over an element are defined, the piecewise linear function with monotonic behaviour are defined as

$$\frac{\partial \phi_L}{\partial x} = \frac{1}{2}(\mathrm{sgn}(s^L) + \mathrm{sgn}(s^R)) \min(|s^L|, |s^R|, |S|) \tag{2.26}$$

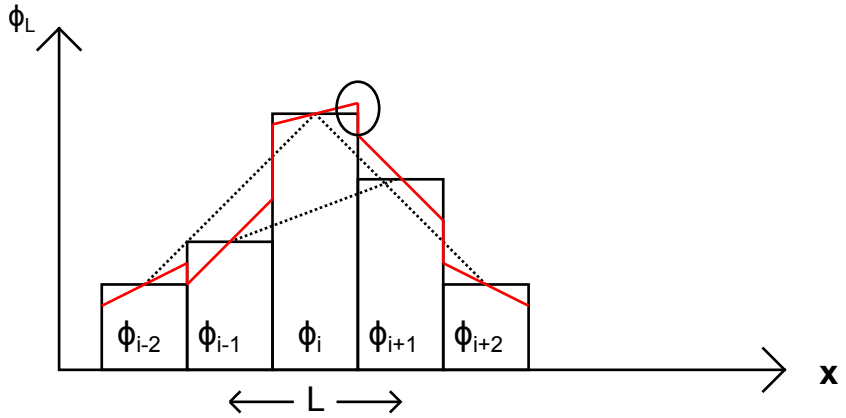

Figure 2.4: *The piecewise linear function ϕ_L is described with red color and the dashed line defines the slope of ϕ_L over an element using the central differencing approach. The circle indicates that a new maximum value is introduced at the position of the circle.*

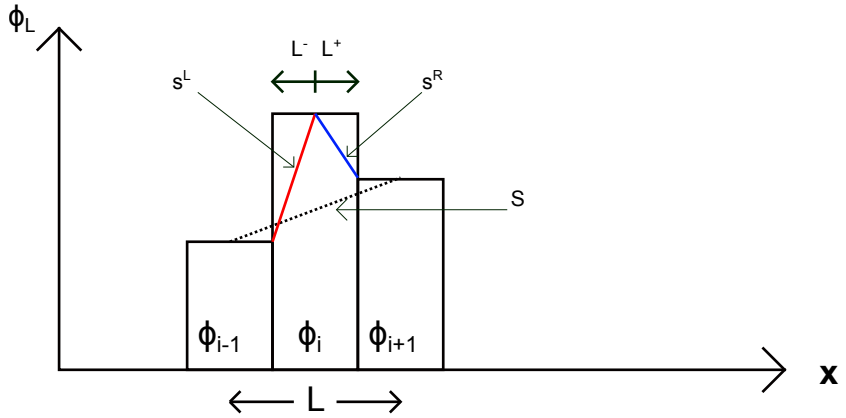

Figure 2.5: *An example of how the maximum slopes at the left (red line), s^L, and right (blue line), s^R and the central differencing slope S are defined for element ϕ_i*

where the sign function sgn is defined as

$$\operatorname{sgn}(x) = \begin{cases} -1 & \text{If } x < 0 \\ 0 & \text{If } x = 0 \\ 1 & \text{If } x > 0 \end{cases} \tag{2.27}$$

2.5 Critical time step size

During time integration in an explicit scheme the time step must be smaller than a specific value to be conditionally stable. This critical time step, Δt_{cr}, is defined by the highest eigenfrequency, $\omega_{\max}$, of the domain

$$\Delta t_{\text{cr}} = \frac{2}{\omega_{\max}} \tag{2.28}$$

The maximum eigenfrequency, $\omega_{\max}$, is computationally expensive to calculate and instead the critical time step, Δt_{cr}, is approximated as

$$\Delta t_{\text{cr}} \approx \min_{\text{nel}} \left[\frac{\Delta x^e}{c}, \frac{\Delta x^e}{4 v^{\text{flux}}} \right] \tag{2.29}$$

where Δx^e is a characteristic element size, c speed of sound and v^{flux} is the flux velocity defined as

$$v^{\text{flux}} = \max_i (||\dot{\mathbf{X}}_i - \mathbf{V}_i||) \tag{2.30}$$

where $\dot{\mathbf{X}}_i$ is the velocity of the material, $\mathbf{V}_i$ the mesh velocity and i indicate the direction of the velocity. With this definition no particles in the system will travel more than half an element cell during one time step which is important for the advection accuracy [19].

2.6 Porosity and permeability

Fabric material is often classified as a porous material, which means that fluid can flow through it. How much fluid that can flow through the porous material depends on the permeability of the fluid in the porous material. In some applications this phenomenon is of great interest and some typical applications are parachute and airbag deployments. The flow through a thin porous media can be described by the Ergun's equation for shells

$$\frac{\Delta p}{t} = A_n(\varepsilon, \mu)v_n + B_n(\varepsilon, \rho)v_n^2 \tag{2.31}$$

where Δp is the pressure drop across the shell with thickness t, A_n is the reciprocal permeability (or viscous coefficient) which consider the viscous effects and is defined by the porosity, ε, of the material and the dynamic viscosity, μ of the fluid. The coefficient B_n is considering the inertial effects and is defined by the porosity of the material and the density, ρ, of the fluid. v_n is the relative velocity in the normal direction between the porous surface and the fluid [16]. The coefficients can be defined as [27]

$$A_n = \frac{150\mu(1-\varepsilon)^2}{D^2\varepsilon^3}; \quad B_n = \frac{1.75\rho(1-\varepsilon)}{D\varepsilon^3} \tag{2.32}$$

where the porosity, ε, is the ratio between the void (empty space) and the total volume of a porous media

$$\varepsilon = \frac{V_{\text{void}}}{V_{\text{total}}} \tag{2.33}$$

D is a characteristic length defined as

$$D = \frac{6(1-\varepsilon)V}{S} \tag{2.34}$$

where V is the volume of the porous media and S is the surface.

As seen in (2.31) the Ergun equation describe the fluid flow through a porous material at a specific pressure difference using two coefficients, A_n and B_n. The permeability is a description of the fluid flow through the porous material at a specific condition while the porosity is a characteristic property of the material [24]. It is often more common to find material data considering the permeability (often a specific volume flow at a specific time span and a specific pressure difference) than porosity for the material [27]. Therefore the coefficients A_n and B_n need to be determined to fit these given permeability data as good as possible.

2.7 Total and static pressure

For incompressible flows the total pressure can be determined by the Bernouilli's equation

$$p_0 = p + \frac{1}{2}\rho v^2 \tag{2.35}$$

where p_0 is the total pressure, p is the static pressure and the last term in eq (2.35) is the dynamic pressure consisting of density, ρ, and velocity, v. Liquid and low speed flows can be assumed to be incompressible. For compressible flows the total pressure can be expressed as [3]

$$p_o = p\left(1 + \frac{\gamma - 1}{2}M\right)^{\gamma/(\gamma-1)} \tag{2.36}$$

where γ is the ratio between the specific heats at constant pressure, C_p, and constant volume, C_v,

$$\gamma = \frac{C_p}{C_v} \tag{2.37}$$

and M is the Mach number of the flow

$$M = \frac{v}{a} \tag{2.38}$$

where a is the speed of sound in the fluid

$$a = \sqrt{\frac{\gamma p}{\rho}} \tag{2.39}$$

For a gas, the speed of sound can be modified with the ideal gas law, $p = \rho RT$

$$a = \sqrt{\gamma RT} \tag{2.40}$$

where $R = C_p - C_v$ and T is the static temperature. It should be notated that for flows with low velocity, $v \to 0$, the total pressure and the static pressure are almost equal

$$p_o \approx p \tag{2.41}$$

2.8 Artificial bulk viscosity

A shock wave gives rise to a discontinuous jump in pressure, density, particle velocity and energy. This kind of discontinuous behaviour often results in numerical issues. To be able to solve this in a computer most wave propagation codes use an artificial bulk viscosity [18]. This artificial bulk viscosity, q, is added to smear the shock so it changes rapidly but in a continuous way. In LS-DYNA this viscosity is defined as

$$q = \begin{cases} \rho l(C_0 l \dot{\varepsilon}'^2_{kk} - C_1 a \dot{\varepsilon}'_{kk}) & \text{If} \quad \dot{\varepsilon}'_{kk} < 0 \\ 0 & \text{If} \quad \dot{\varepsilon}'_{kk} \geq 0 \end{cases} \tag{2.42}$$

where C_0 and C_1 are dimensionless constants, a is the speed of sound, ρ is the density, $l = \sqrt[3]{V}$ is a characteristic length based on the element volume V and $\dot{\varepsilon}'_{kk}$ is the trace of the strain rate tensor defined in eq (2.6).

3 Simulation set-up

In this thesis the Finite Element based software LS-DYNA was used to create the model and to perform the calculations. The simulations ran on a computer with 128 GB RAM and 16 cores. Several models have been made to evaluate how different parameters affect the acceleration of the bag. A case that was representing a clean bag at typical standard conditions was first made as a reference case. In the other cases only one parameter was changed compared to the reference case. The study included:

- Different permeability of the bag
- Different weight of the dust cake

The simulations did not include dust particles in the flow. Only the dust that got stuck on the bag were included as an extra weight on the bag. Also it was not possible to model turbulence in the MMALE method and no account for boundary layer effects could be made [7]. All commandos used in the different cases could be seen in Appendix C.

3.1 Geometry and model dimensions

All models contained the same parts with the same dimensions. All models included a nozzle, bag plate, bag, cage and three air domains. One air domain represents the air below the bag plate, one the air between the bag plate and the nozzle inlet and the last represents the air in a tank. The dimensions of the geometry could be seen in Figure 3.1 and 3.2 where $D = 0.129\,\text{m}$, $d = 0.04\,\text{m}$ and $L = 10\,\text{m}$. The cage consisted of eight rods

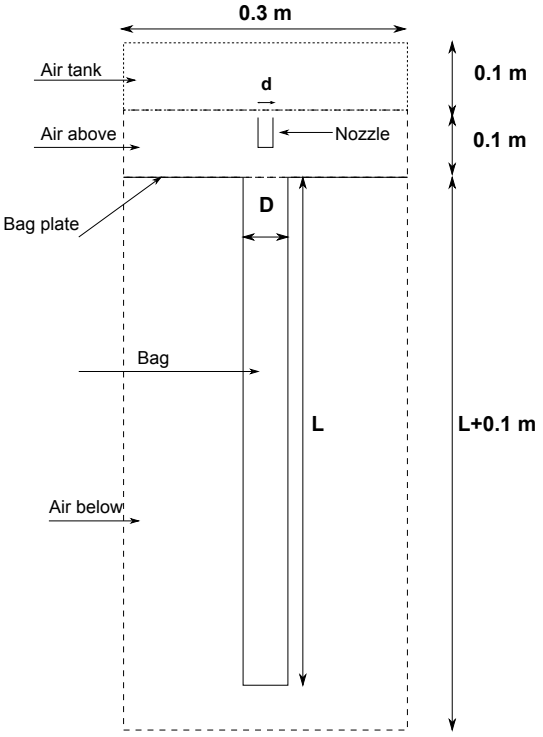

Figure 3.1: *Side view of the model geometry with cage parts excluded.*

equally spaced on the inside of the bag and a plate, with slightly smaller dimensions than the bag, located near the bottom of the bag. The cage prevented the bag from crumpling when the air flowed through the filter. The cage parts could be seen in Figure 3.3 together with the bag plate and the bag and by itself in Figure 3.4. The cage parts were located in such a way that it initially existed a gap of 1 mm between the bag and the cage parts. This was done to prevent initial penetration which could lead to non-physical accelerations in the bag.

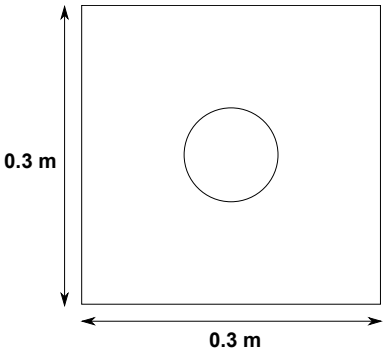

Figure 3.2: *Top view of the model geometry with cage parts excluded.*

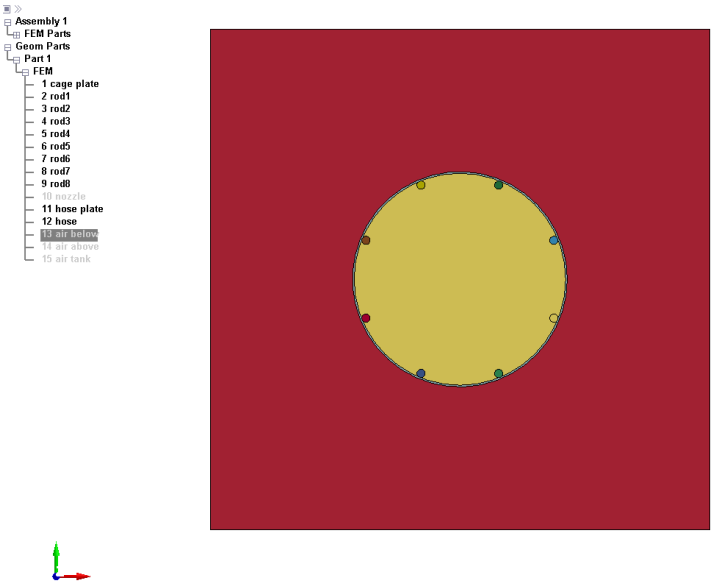

Figure 3.3: *A top view where eight rods, a plate (yellow) belonging to the cage structure and the bag plate (red part) could be seen*

The center of each rod was determined with eq (3.1)

$$\begin{aligned} x_n =& \frac{d_c}{2}\cos(an+\phi) \\ y_n =& \frac{d_c}{2}\sin(an+\phi) \end{aligned} \tag{3.1}$$

where

$$\begin{aligned} a =& \frac{2\pi}{n_r} \\ d_c =& (D-0.002)-2r_c \\ \phi =& \frac{a}{2} \end{aligned} \tag{3.2}$$

and the origin coincided with the center of the bag. In eq (3.1) n goes from $0 \rightarrow (n_r - 1)$ where n_r denotes the number of rods and in eq (3.2) r_c denotes the radius of the rods. The radius of the rods were $r_c = 2.5\,\text{mm}$.

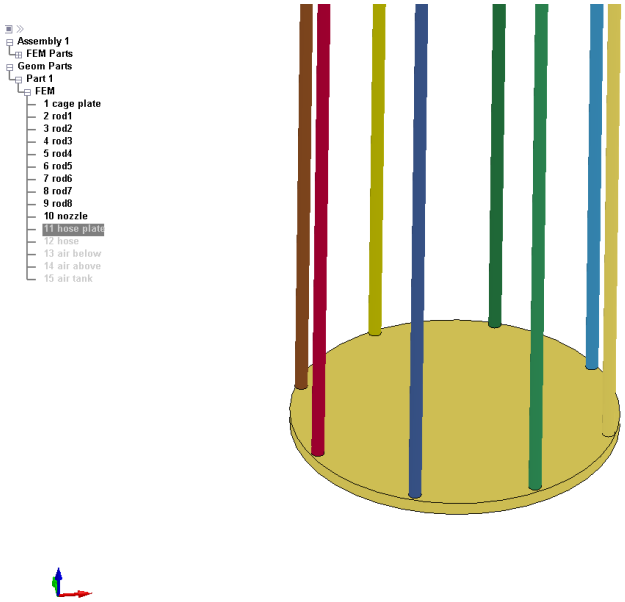

Figure 3.4: *A view of the lower parts of the rods and the plate*

3.2 Part modelling

The parts in the different cases were modelled in the same way but with different values. Each part were defined by Lagrangian or ALE formulation, section, element formulation, material type. If the material type was defined as a null material also an equation of state needed to be defined. The part definitions could be seen in Table 3.1. The rigid and null materials were the same in all cases. The thickness of the rigid shell sections

Table 3.1: Part definitions used in the different cases

Part	**Formulation**	**Section**	**Element formulation**	**Material**	**Equation of state**
Air above	ALE	Solid	1 point MMALE	Null	Ideal gas
Air below	ALE	Solid	1 point MMALE	Null	Ideal gas
Air tank	ALE	Solid	1 point MMALE	Null	Ideal gas
Bag	Lagrangian	Shell	Belytschko-Tsay membrane	Fabric	-
Bag plate	Lagrangian	Shell	Belytschko-Tsay	Rigid	-
Cage plate	Lagrangian	Solid	Constant stress element	Rigid	-
Cage rods	Lagrangian	Solid	Constant stress element	Rigid	-
Nozzle	Lagrangian	Shell	Belytschko-Tsay	Rigid	-

was 3 mm and the defined material properties for the rigid material were the density, ρ, Young's modulus, E, and Poission's ratio, ν. The rigid material was defined as steel and the steel properties used could be seen in Table 3.2. Even if a part was defined as a rigid material it was important to define proper material data due to that LS-DYNA used the material properties to calculate a contact stiffness. Also, the meshes of the rigid bodies were only used to define the geometries of the parts. Elements belonging to a rigid part was bypassed in the element processing and no variables were stored [17].

Table 3.2: Material properties of rigid steel

Material	**Density, ρ, [kg/m^3]**	**Young's modulus, E, [GPa]**	**Poisson's ratio, ν**
Rigid	7800	210	0.3

The null material is a material without shear stiffness (except viscosity if any) [17]. The use of null material required an equation of state and in this thesis the ideal gas law was used. This material suits well for

fluid-like materials. This material model was used to model the air and the properties defined were the density, ρ, and the dynamic viscosity, μ. These properties could be seen in Table 3.3. The properties of the equation of state for the standard condition (SC) could be seen in Table 3.4. The standard condition of the equation of state were used in all cases.

Table 3.3: Material properties for the null material

Material	**Density, ρ,** [kg/m^3]	**Dynamic viscosity, μ,** [Pa $\cdot$ s]
Null	1.2	$1.85 \cdot 10^{-5}$

Table 3.4: Equation of state properties at standard conditions (SC)

Equation of state	C_v, [J/(kg $\cdot$ K)]	C_p, [J/(kg $\cdot$ K)]	**Temperature,** [K]	**Relative volume,** ρ_o/ρ
Ideal gas (SC)	717	1004	295	1

The bag[1] was modelled with a fabric material. This material was only supported for 3 or 4 nodes membrane elements [17] and this was the reason why this model ran as a 3D model instead of an axisymmetric 2D model. The strain formulation used in the fabric model was the Green-Lagrange strain formulation due to that relatively large deformation could occur. The properties defined for the fabric were the density, Young's modulus, Poisson's ratio and Ergun's coefficients (to consider the permeability of the bag, see eq (2.32)). The fabric was assumed to behave isotropic due to that deformations were mainly expected to occur in radial direction due to influence of the cage bottom plate (no air could flow through the cage plate and therefore most air would leave the bag in the radial direction). Both the density, ρ, and the Ergun's coefficients A_n and B_n needed to be calculated from known data. For the bag the area density, ρ_A, i.e mass per unit area was known and the following equation was used to calculate the density ρ of the bag

$$\rho = \frac{\rho_A}{t} \tag{3.3}$$

where t was the thickness of the bag. Also the permeability was known for a specific pressure drop. It was assumed that the pressure drop had a linear relation to the flow velocity[2] and therefore the inertial coefficient, B_n, could be put to zero and only the viscous coefficient, A_n, was determined. Here an arbitrary value q denotes the value of the permeability, v_n

$$v_n = q \, \frac{\text{liters}}{\text{dm}^2 \cdot \text{minute}} \tag{3.4}$$

The unit in eq (3.4) needed to be consistent and was rewritten to SI units and this resulted in

$$v_n = \frac{q}{600} \frac{\text{m}}{\text{s}} \tag{3.5}$$

Equation (3.5) in eq (2.31) gave

$$A_n = \frac{\Delta p}{t \cdot v_n} = 600 \frac{\Delta p}{t \cdot q} \tag{3.6}$$

The properties of the bag differed between the cases and are instead presented under respective case rather than here.

3.3 Boundary conditions and loads

For a given problem the boundary conditions and loads must be defined for the parts in the model. All inflow/outflow boundaries were set to be non-reflecting boundaries to avoid reflection when the air was flowing out of the domain. An alternative way to the non-reflecting boundaries could have been the use of an extra layer of AET (Ambient element type) on the boundaries of the domain [30]. The AET option could be found in the element formulation and if it was used it defined the ambient conditions. The walls of the tank were modelled with *ALE_ESSENTIAL_BOUNDARY where it was defined that no fluid could flow through the walls.

[1] PPS/PPS 554 glaze CS31 bag

[2] It is a quite linear correlation, as flow is very laminar inside the bag, according to the supplier at BWF Envirotec

Pressure loads on the ALE parts

The initial flow in the models resulted from a pressure difference, Δp, between the air above and below the bag plate. Due to that the compressible solver was used it was not sufficient to just define the pressure difference but also the absolute pressure was needed. The atmospheric pressure, p_{atm}, was set to be 100 kPa in all cases. The pressure below the bag plate, p_1, was set to be the atmospheric pressure plus the pressure difference

$$p_1 = p_{\text{atm}} + \Delta p \tag{3.7}$$

and the pressure above the bag plate, p_2, was set equal to the atmospheric pressure

$$p_2 = p_{\text{atm}} \tag{3.8}$$

In reality a big tank was emptied and the flow was distributed over several nozzles and bags, but it was too computer demanding to consider all of them. Instead of simulating a full scale tank a pressure boundary condition was used. The total pressure, $p_0(t)$, at the nozzle was known and was applied as a boundary condition

$$p_0(t) = p_{\text{atm}} + p_{0,\text{over}}(t) \tag{3.9}$$

where the overpressure, $p_{0,\text{over}}(t)$, was the same for all cases. Since it was unclear whether LS-DYNA used total pressure or static pressure at the boundaries the total pressure boundary condition was defined on a much bigger surface than the nozzle inlet. This due to that the inflow velocity is much lower on a large surface and with this in mind it was assumed that $p_o \approx p$ on the larger surface. The applied pressure loads could be seen in Figure 3.5. The overpressure at the boundary was ramped up to its peak value, $p_{\max}$, in 2 ms from which it decreased linearly for 300 ms until it reached a value of (1/8) of $p_{\max}$ where it was ramped down to zero. Compared with the experiment this was a simplification that still was quite close to the reality. The peak value was 150 kPa for all cases. The shape of the overpressure pulse could be seen in Figure 3.6.

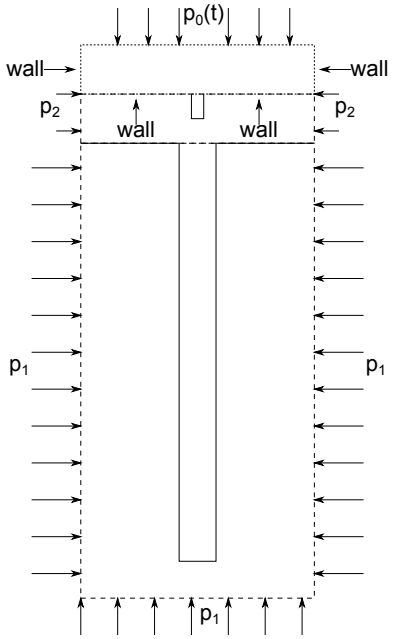

Figure 3.5: *The geometry of the model with the applied pressure loads on the air domain*

Boundary conditions of the Lagrangian parts

All the degrees of freedom for the rigid parts (nozzle, bag plate, cage parts) were locked in space, i.e they could not move or rotate. The bag itself was mounted on the bag plate and only the degrees of freedom at the location of contact were locked. This could for example be seen in Figure 3.1.

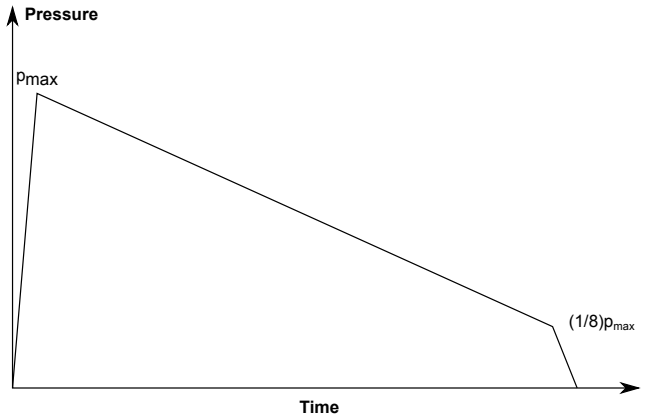

Figure 3.6: *The applied overpressure was ramped up to p_{max} in 2 ms from which it decreased linearly for 300 ms until it reached a value of (1/8) of p_{max} where it was ramped down to zero*

3.4 Contact definitions

The load on the bag was not constant during the simulations due to the interaction between the bag and the cage and also due to the flow interaction. To include the contact load from the cage on the bag a contact algorithm had to be used. The contact algorithm used in this thesis was the *ONE_WAY_SURFACE_TO_SURFACE which defined the contact between the bag and the cage parts. The algorithm searched for penetration between the parts for which the contact was defined for and if a penetration was found a force proportional to the penetration distance was applied at the nodes to eliminate the penetration (i.e a penalty based contact). Also, the interaction between the flow and the bag gave rise to loads on the bag. Due to that the air and the bag were formulated with different formulations (ALE and Lagrangian formulations) there were a special type of contact. When ALE or Eulerian parts interact with Lagrangian parts a fluid-structure interaction coupling must be defined [7]. The coupling used was the *CONSTRAINED_LAGRANGE_IN_SOLID in which the Lagrangian part needed to be defined as a slave part and the solid parts (ALE) were defined as the master. Also in the *CONSTRAINED_LAGRANGE_IN_SOLID there were different coupling types (CTYPE) to chose between but here a coupling type that considered the permeability (CTYPE=11) of the Lagrangian part (the bag) was used. This coupling type used a penalty based formulation. Also, the Ergun's viscous coefficient, A_n, was defined under this option.

3.5 Cases

To account for the initial flow in the simulations, the overpressure at the nozzle was applied when a relatively "steady" initial solution was achieved. For these models a time of 0.1 s was used. The MMALE solver in LS-DYNA, which is a compressible solver, was used in the simulations.

The mesh was the same for all cases. The air domains were build up of solid boxes with the shape mesher tool in LS-DYNA. The element size of the air domains was 0.01 m in all directions which resulted in a total of 927 000 elements for the air domains. This element size was considered to be the smallest size with acceptable computational time. The air mesh could be seen in Figure 3.7. Also the rods were made in the shape mesher tool but using a cylindrical shape. The cage parts had together 177 364 elements but these were only used to define the geometry and material for the cage parts. The other parts were meshed with the auto mesher tool with an approximative element size of 0.01 m. This resulted in 65 elements for the nozzle, 721 elements for the bag plate and 41 170 elements for the bag. The nozzle, bag plate, rods and bag meshes could be seen in Figure 3.8.

Regarding the material data of the bag, the Poission's ratio was unknown. In [12] it was shown that the Poission's ratio varied exponentially as a function of the extension in a fabric material. It was also dependent on which direction of the fabric that was considered. But in LS-DYNA it was only possibly to define one value in each direction and since the fabric was approximated as an isotropic material (due to that the bag

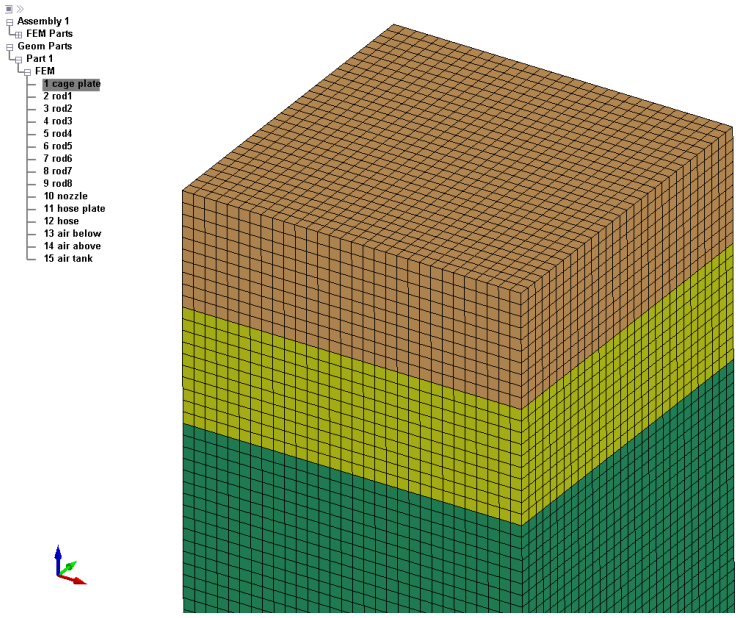

Figure 3.7: *Mesh of the air domains for all cases*

displacements only were expected in crosswise direction) only one value on the Poisson's ratio was used. The Poisson's ratio was set to $\nu = 0.14$ as this value was used in a parachute simulation [27]. The thickness, t, and Young's modulus, E, were the same for all cases, 1.7 mm and 39.2 MPa, respectively.

The advection scheme used in the simulations was the Van Leer algorithm due to that it was more accurate than the Donor Cell algorithm. The Donor Cell algorithm was considered to be too dissipative and dispersive.

3.5.1 Reference case

The reference case was representing a clean bag at standard conditions. The results from the other cases were compared to this case. In this reference case the maximum pressure, $p_{\max}$, (see Figure 3.6) was 150 kPa and the pressure difference was $\Delta p = 1500$ Pa. The bag had the following material data; Young's modulus $E = 39.2$ MPa, weight of bag $\rho_A = 0.550\,\mathrm{kg/m^2}$, dust cake weight $\rho_D = 0\,\mathrm{kg/m^2}$ and the permeability v_n at 200 Pa was 120 liters/(dm^2 · minute). To be able to implement the model in LS-DYNA, ρ_A and ρ_D must be expressed as material (volume) density ρ. The bag weight was transformed to density using eq (3.3) which gave $\rho = 323.5\,\mathrm{kg/m^3}$. For a non-zero value on the dust cake weight this weight would have been added to the bag weight before using eq (3.3). Also the permeability needed to be defined as the Ergun's viscous coefficient, A_n. To determine A_n eq (3.6) was used which gave $A_n = 588\,235\,(\mathrm{Pa \cdot s})/\mathrm{m^2}$.

3.5.2 Other cases

Compared to the reference case only one parameter was changed for each case. This was done to see how much a specific parameter influenced the bag dynamics. Which case that considered which parameter can be seen in the list below:

- Case 1 and 2 considered different permeability
- Case 3 and 4 considered different dust cake weight

A summarized table containing all the cases could be seen in Table 3.5. Also the result of the necessary transformations could be seen in Table 3.6.

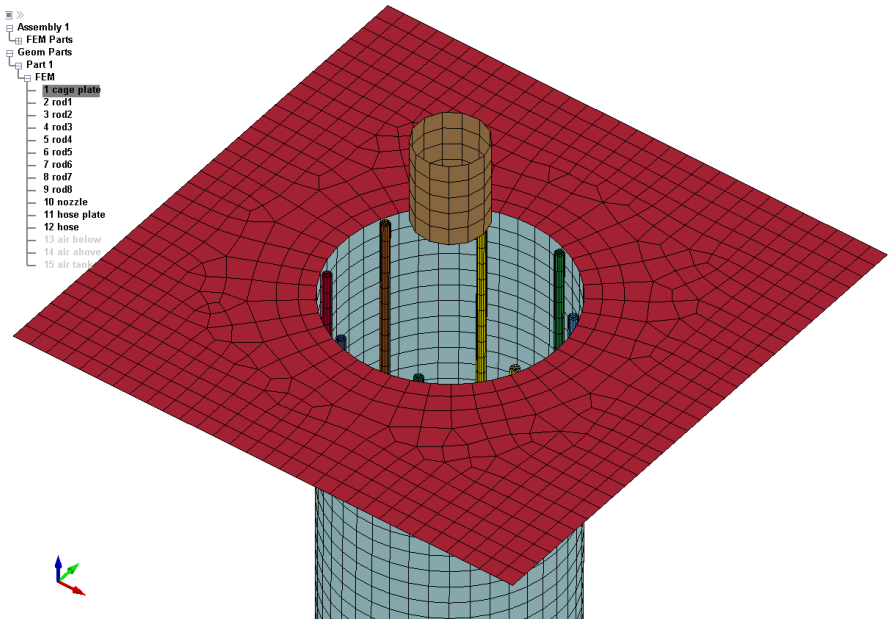

Figure 3.8: *Meshes of the nozzle, bag plate, cage rods and bag*

Table 3.5: Definitions of the used values for different parameters in the different cases

Case	$p_{\max}$ [kPa]	E [MPa]	ν	$\rho_A + \rho_D$ [kg/m^2]	Δp [Pa]	v_n [liters/(dm^2 · minute)], $\Delta p = 200\,\text{Pa}$
Reference	150	39.2	0.14	0.550	1500	120
1	150	39.2	0.14	0.550	1500	60
2	150	39.2	0.14	0.550	1500	30
3	150	39.2	0.14	1.550	1500	120
4	150	39.2	0.14	3.550	1500	120

Table 3.6: The density and Ergun's coefficient for the different cases

Case	ρ [kg/m^3]	A_n [(Pa · s)/m^2]
Reference	323.5	588 235
1	323.5	1 176 471
2	323.5	2 352 941
3	911.8	588 235
4	2088.2	588 235

4 Result

In this chapter the results are presented. Some graphs look strange due to that there was some problem with viewing the results in the post-processor. There were some intervals where the results were missing which made it hard to analyse the results. The reason for the problem was unknown, but probably it had something with the hardware due to that LSTC did not have any problems when running the keyword-file on their computers.

4.1 Comparison with experiments

Some experimental results did exist and the data have been used to see how the ALE simulation of the bag predicted this kind of physics. The known data were the total mass flow into a bag, pressure near the bag surface and how long time it took for the pressure pulse to reach the cage plate located in the bottom of the bag. Most of the experimental results and the experiment set-up was confidential and could not be sheared in this thesis. In this section the results from the simulation of a clean bag were compared with these known experimental data.

4.1.1 Mass of the inflowing air into a bag

To clean the bags a high pressure tank was emptied. The pressurized air was directed to the bags by several nozzles. When the tank opens, the air flows from the tank to the nozzles until the pressure in the tank reaches atmospheric pressure i.e the mass representing the overpressure flows out of the tank. The mass of the air flowing out of the tank could be calculated as

$$m_{\text{tank}} = \rho_{\text{tank}} V_{\text{tank}} \tag{4.1}$$

and together with the ideal gas law this could be expressed as

$$m_{\text{tank}} = \frac{p_{\text{tank}}}{RT} V_{\text{tank}} \tag{4.2}$$

where m_{tank} is the mass, p_{tank} is the tank overpressure, R is the gas constant for air, T is temperature and V_{tank} is the tank volume. The volume that this mass occupies in atmospheric conditions can be calculated as

$$V_{\text{atm}} = \frac{m}{\rho_{\text{atm}}} \tag{4.3}$$

where ρ_{atm} is the density in atmospheric conditions. This resulted in that 32.3 liters of air at atmospheric conditions was flowing into each bag. This value could be checked against the value of the mass flow in the model. A function that calculates the mass flow through a surface in LS-DYNA was not found so an approximation of the mass flow has been made instead. The mass flow rate can be expressed as

$$\dot{m} = \rho v A \tag{4.4}$$

where $\dot{m}$ is the mass flow rate, ρ is the density of the air, v is the velocity of the air at the nozzle inlet and A is the area of the nozzle. The velocity was assumed to behave linearly (same behaviour as the pressure at the nozzle) and to simplify the approximation a mean value of the velocity, $\bar{v}$, was used. The velocity used was

$$\bar{v} = \frac{v_{\max} + v_{\min}}{2} \tag{4.5}$$

The velocities used in eq (4.5) was chosen to be $v_{\max} = 170\,\text{m/s}$ and $v_{\min} = 0\,\text{m/s}$. The maximum velocity was motivated by that this was the highest velocity of the inflowing air, as can be seen in Figure 4.1 and the minimum value will be zero when the tank pressure has reached atmospheric conditions. Also the density varied during the inflow and the mean value was put to be $1.25\,\text{kg/m}^3$. Using eq (4.4) with nozzle diameter, $d = 0.04\,\text{m}$, gives the average massflow rate through a nozzle as

$$\bar{\dot{m}} = 0.133\,\text{kg/s} \tag{4.6}$$

The total mass flow through a nozzle during the cleaning was (time t for the cleaning was approximately 300 ms)

$$m = \bar{\dot{m}} \cdot t = 0.0398\,\text{kg} \tag{4.7}$$

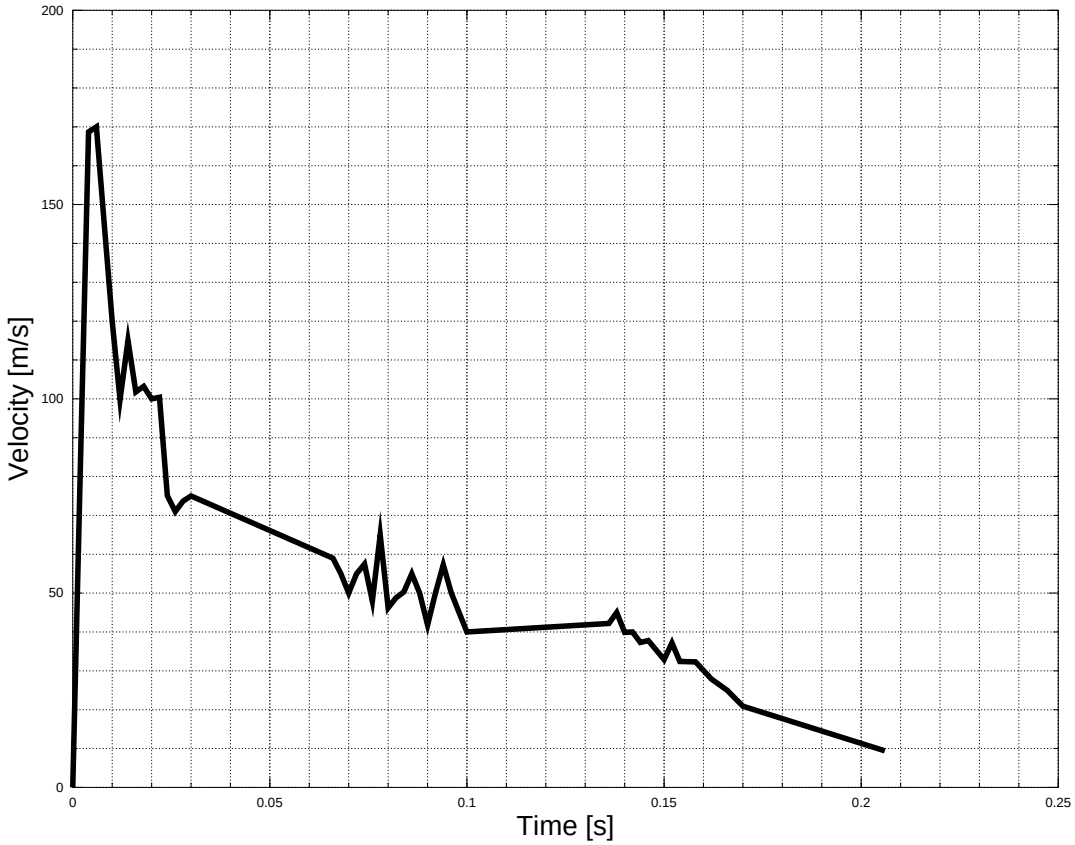

Figure 4.1: *The velocity of the propagating air inside the bag. The velocity was measured until the air reached the bottom of the bag.*

This mass occupy a certain volume, but here the volume at standard conditions will be used to be able to compare with the theoretical derived result. The volume was calculated as

$$V = \frac{m}{\rho_{\text{standard}}} = 0.0332\,\text{m}^3 = 33.2\,\text{liters} \tag{4.8}$$

where the standard density was $\rho_{\text{standard}} = 1.2\,\text{kg/m}^3$. This corresponds quite well to the derived result. This means that there was a high probability that the right amount of air was flowing into a bag during the cleaning process.

4.1.2 Pressure at the bag surface

The pressure at the bag surface for the reference case could be seen in Figure 4.2, where the zero level was the pressure during the initial flow. The increase in pressure in the lower part of the bag was approximately $400 - 500\,\text{Pa}$ and approximately $1850\,\text{Pa}$ in the upper part of the bag. These peak pressures were significantly lower than the experimental results. The ratio between the peak in the top and the peak in the bottom was approximately $3.7 - 4.6$ which was a bit high compared to the experiment. In Figure 4.3 a trend curve was introduced together with the peak pressure values. These values were scaled in such way that the peak value at the top of the bag (where it was mounted) was equal to 1. The behaviour of the peak pressure looked exponential and the equation of the trend curve was calculated to be

$$y = \text{e}^{-0.1801x} \tag{4.9}$$

where y is the scaled pressure value and x is the distance measured from the top. In Figure 4.2 it could also be seen that the pressure smeared out more further down the bag. To see how the pressure smeared out a pulse

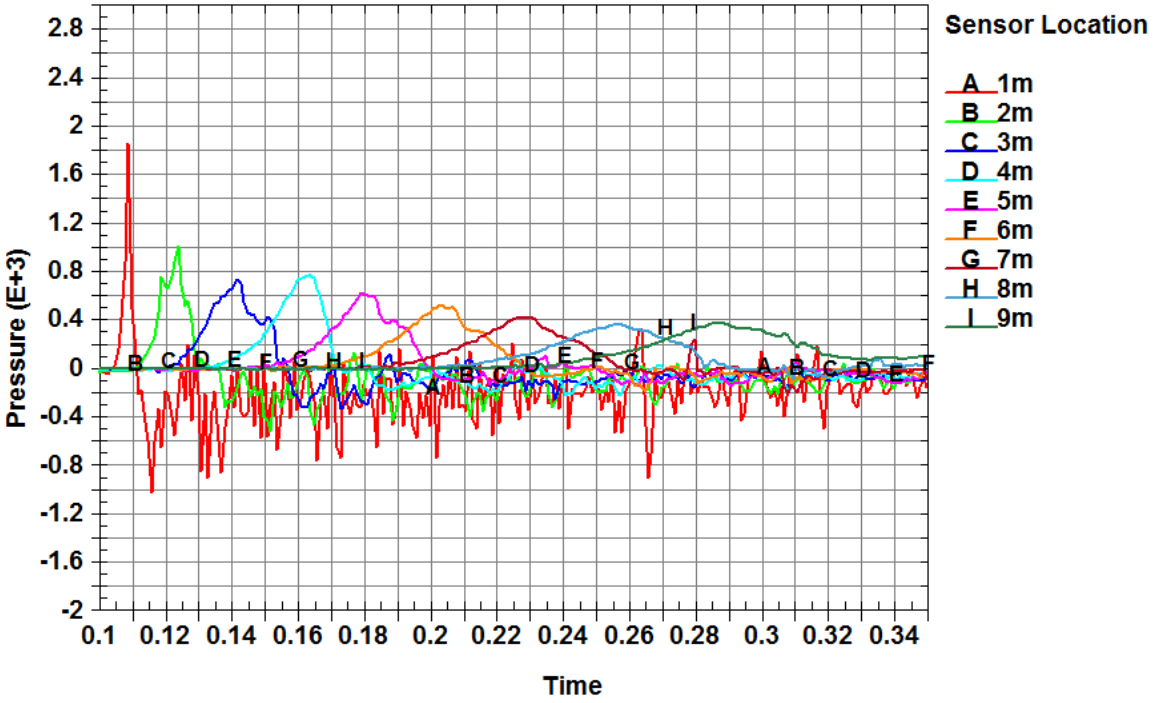

Figure 4.2: *The pressures on the bag surface as a function of time for the clean bag. The zero pressure level represent the pressure levels just before the cleaning started.*

width was measured. The definition of the pulse width are illustrated in Figure 4.4. The pulse width varied linearly with the propagating distance, which can be seen in Figure 4.5.

In the simulation the pressure reached the cage plate in 168 ms which was slightly faster than the inflowing mass, which reached the bottom in 206 ms. The pressure propagation was significantly slower compared to the experiment. Since the results differed from the experiment, a simulation with similar set-up as the experiment was made to see if these results would agree better with the experimental results. The pressures near the bag surface in this case could be seen in Figure 4.6. Even in this case the simulation results did not agree with the experimental values. The pressure pulse reached the bottom cage in 148 ms after injection and the inflowing mass reached the bottom approximately at the same time as for the reference case which still was to slow compared to the experiment. There was an increase in pressure compared to the reference case, but still it was way to low compared to the experimental results.

The problem with the pressure propagation probably has something to do with the pressure boundary condition. A simulation in which no air could flow through the nozzle until the cleaning started was also made. In this simulation the air inside the Air Tank part was pressurized with the $p_{\max}$ value and the nozzle inlet had a wall boundary condition until the cleaning started. When the cleaning started the wall was deleted. In this simulation the pressure propagated much faster than the mass flow. It propagated with the speed of sound approximately for 4-5 m before it loosed its strength, which it still should not do according to the experiments. Also, this simulation later got some numerical errors which resulted in that the simulation diverged.

Due to time limitations, it was decided to continue with some parameter studies on the bag even if the pressures did not match the experiments. The dynamic was only considered at one location, 1 m downward the bag. This was done due to that a rapid change in pressure could be seen at this location (see Figure 4.2 and 4.6), which could be quite representative when simulating this kind of problem. Also, due to that the post-processor skipped some states, it was hard to analyse the result further down the bag. Since only the top was analysed the simulations was shorten, which made it possible to include more simulations in the study. But since the values of the pressure was not totally correct the results was only compared relatively to the

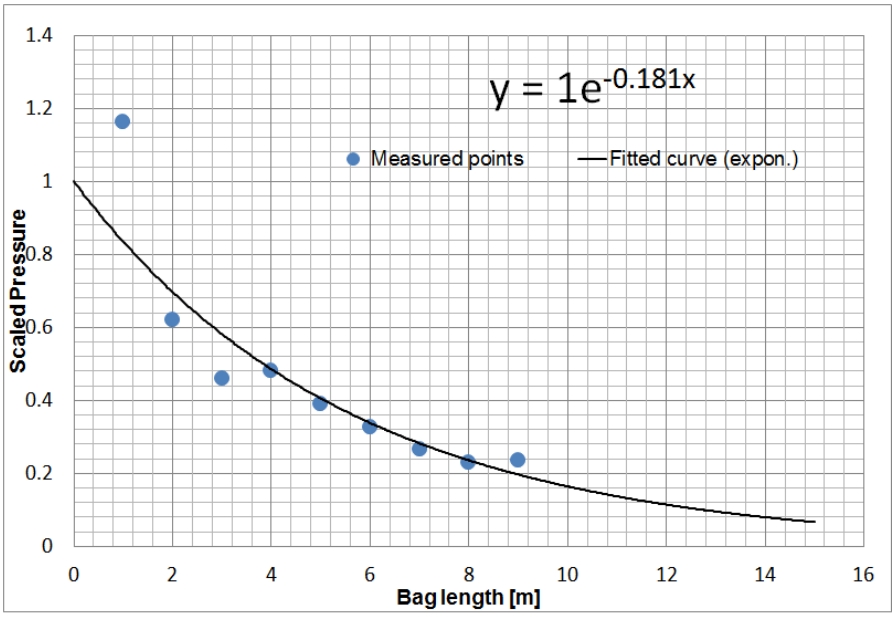

Figure 4.3: *Scaled pressure as a function of the position downward the bag*

clean bag (the reference case). The results should not be taken as true results but more as indications about how different parameters may affect the dynamics of the bag.

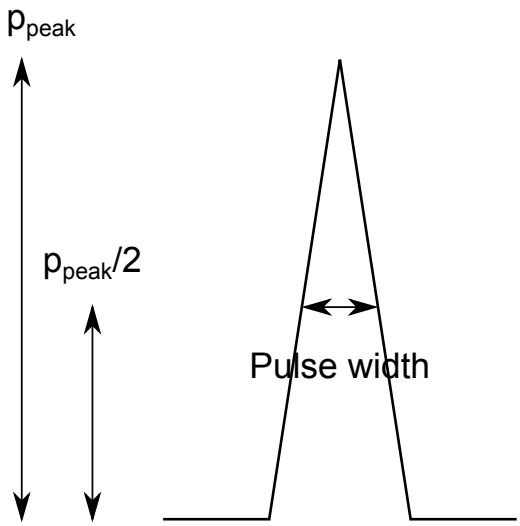

Figure 4.4: *Definition of pulse width*

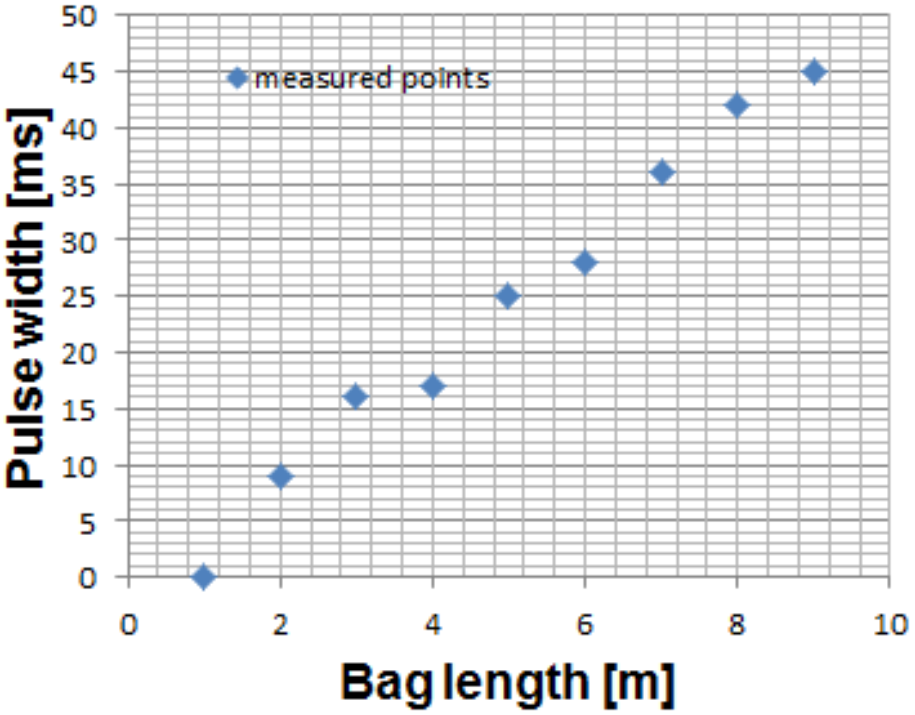

Figure 4.5: *The pulse width as a function of the position downward the bag*

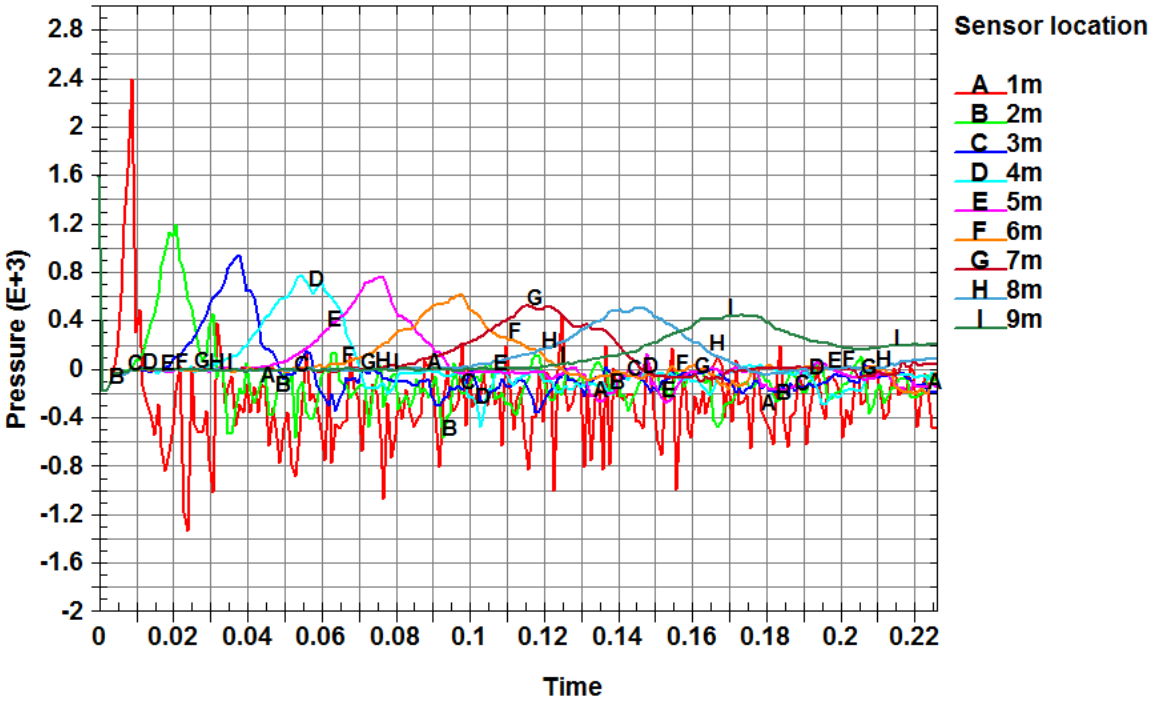

Figure 4.6: *The pressures as a function of time for a simulation with the same set-up as the experiment. The zero pressure level represent the pressure just before the cleaning started.*

4.2 Reference case

The reference case representing a clean bag was used to compare the relative change between the different cases. This was done to see how the cases differed when some specific parameter was changed. The main area of interest was to see how the bag was affected during the cleaning. To get a better understanding of the dynamics of the bag, also the flow was analysed.

4.2.1 Flow characteristics

Before the cleaning process was started the simulations ran for 0.1 s to get an initial flow field. This initial flow field could be seen in Figure 4.7 as vertical velocity (z-velocity). When the air flowed through the bag it was

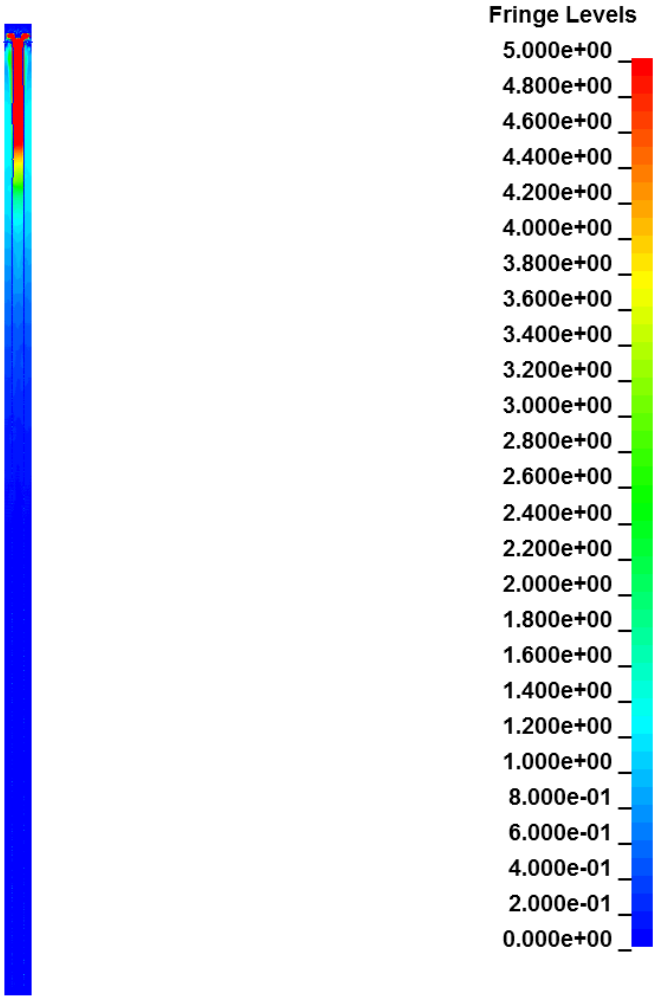

Figure 4.7: *The initial flow viewed as vertical velocity in the flow domain*

accelerating towards the opening at the bag top. This was because the pressure above the bag plate was lower than below the bag plate. The maximum velocity at the bag top was approximately 30 m/s. The most of the air was flowing into the bag at the top. This was because of that the pressure on the inside of the bag at the top was lower than far downward the bag due to the low pressure region above the bag plate. The pressure at the initial state at the top of the bag could be seen in Figure 4.8.

When the cleaning started, air was injected in negative z-direction (opposite direction of the initial flow). The inflowing air needed to change the direction of the initial flow. The injection also resulted in an expansion of the bag, which will be discussed later. The pressure at the moment of injection could be seen in Figure 4.9 and 4.10. The injection of air during the cleaning process results in an increase of pressure in the front of the

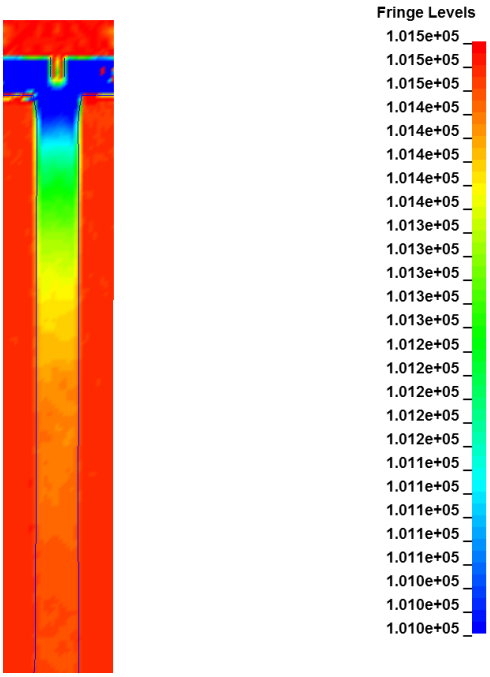

Figure 4.8: *The initial pressure in the flow field at the top of the bag*

inflowing air. After the high pressure region a region with lower pressure occur (blue region in Figure 4.10). This low pressure region occurred inside the bag and outside the bag the pressure was higher. This pressure difference made the bag crumple even if the air from the cleaning still was flowing in. The injected air was mainly flowing downwards but as the air was propagating down the bag some air was flowing through the bag. This is illustrated in Figure 4.11 where the velocity outside the bag was increasing when the air passed by. Figure 4.12 to 4.14 illustrate the air propagating downward the bag.

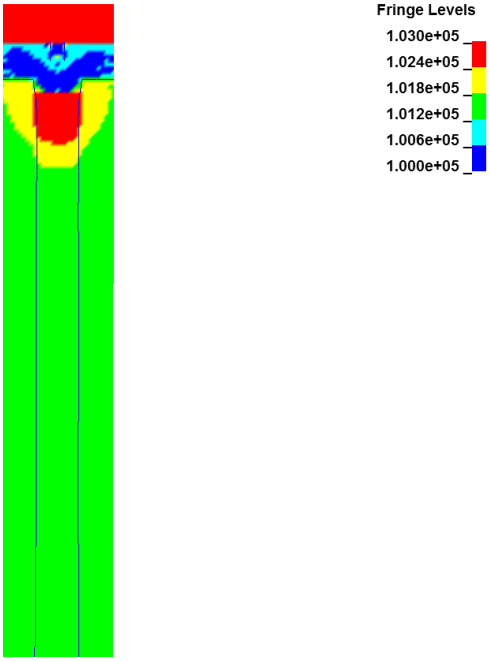

Figure 4.9: *The pressure at the bag top 2ms after the air injection*

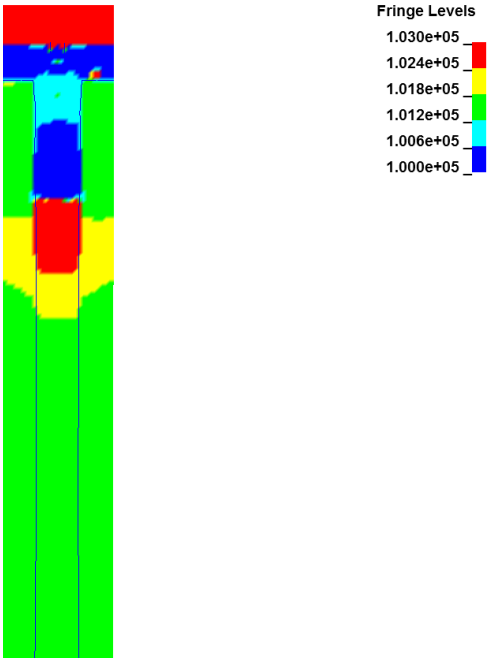

Figure 4.10: *The pressure at the bag top 4ms after the air injection*

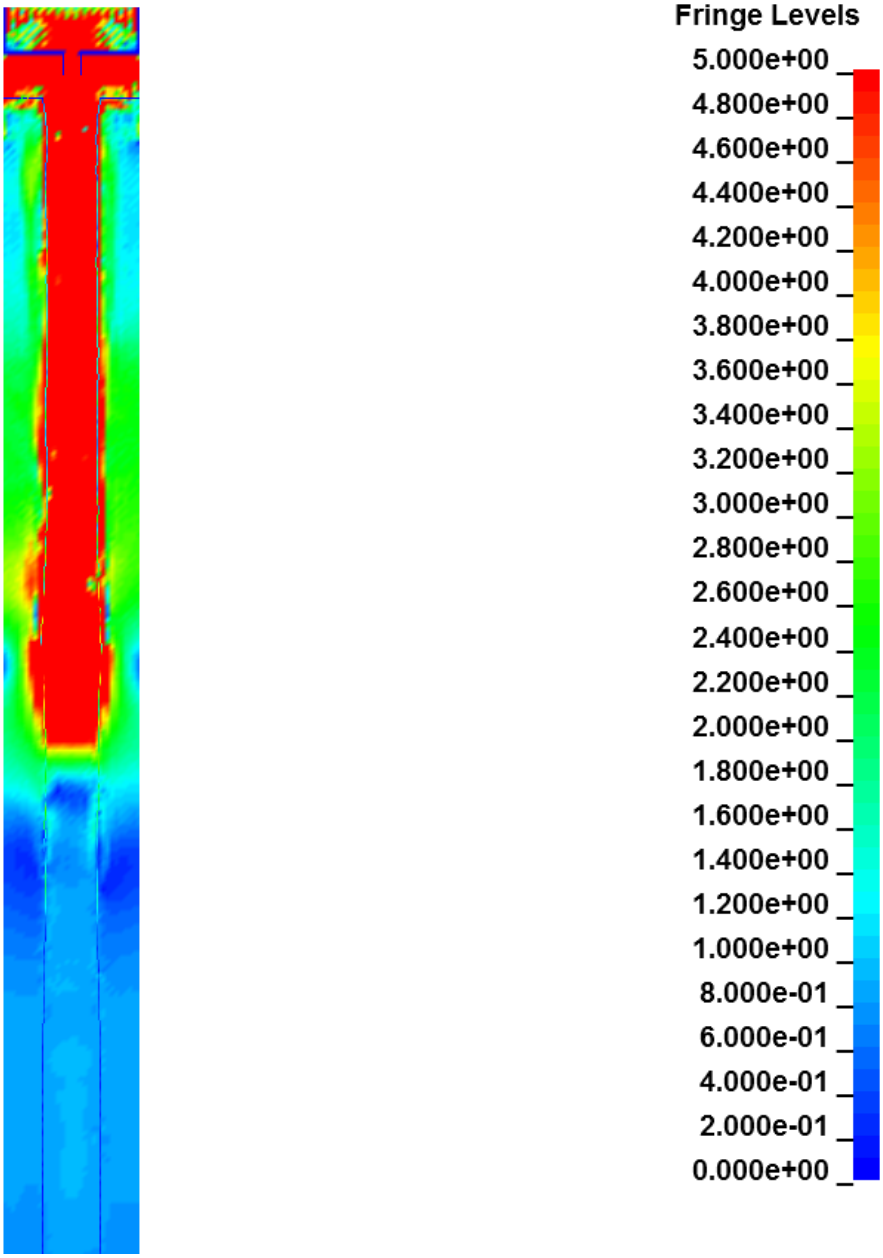

Figure 4.11: *Resultant velocity in the top of the bag 12ms after the air injection*

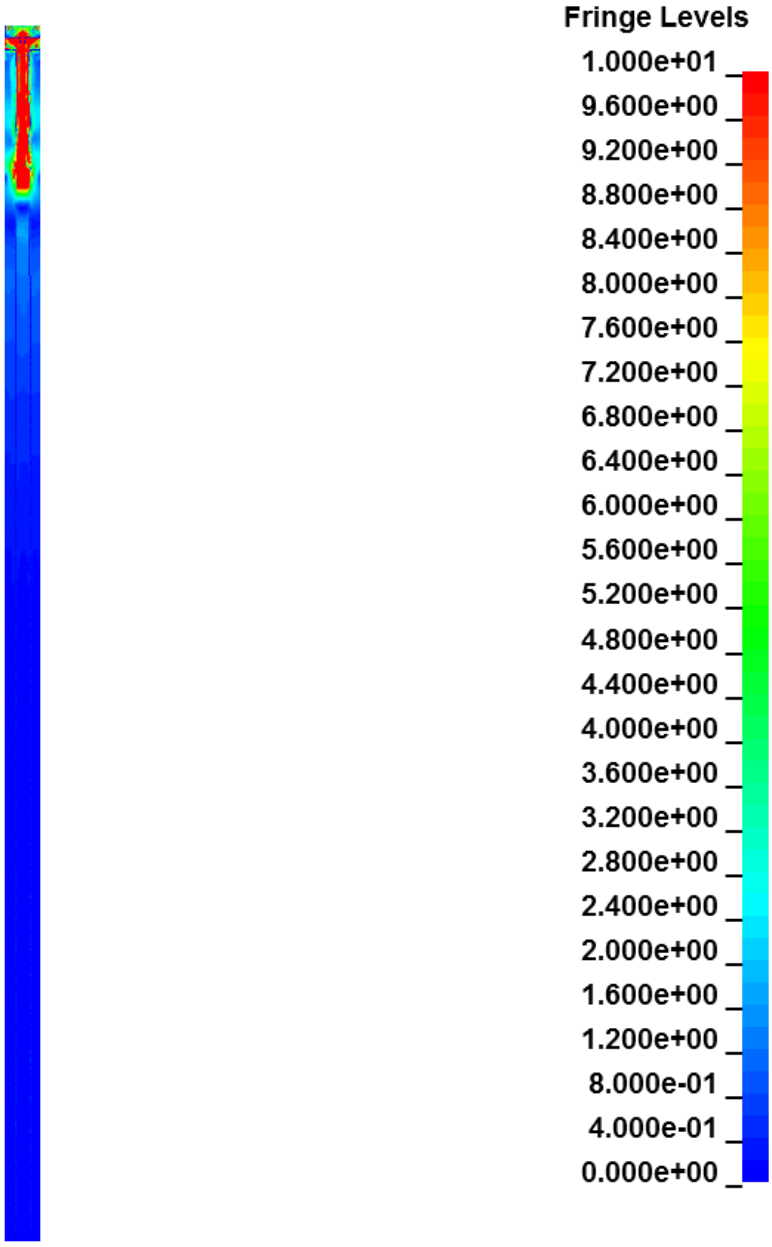

Figure 4.12: *The resultant velocity 10 ms after the air injection*

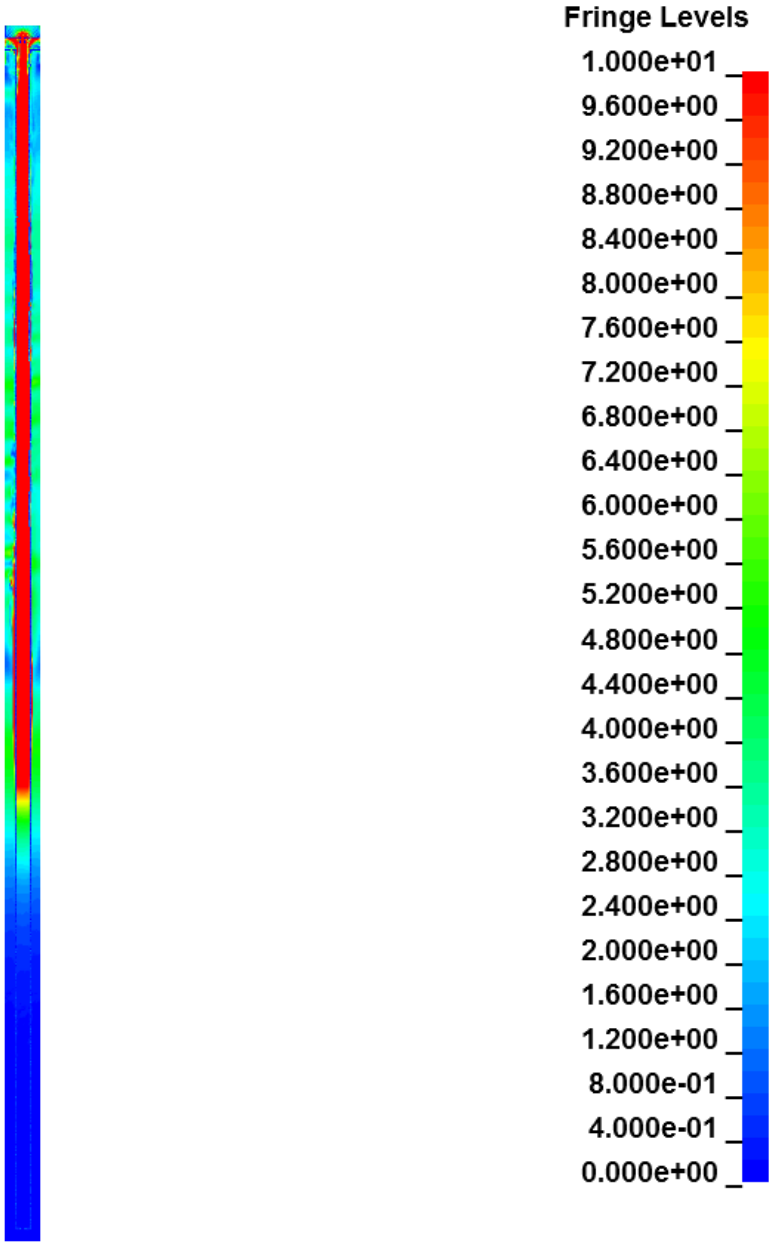

Figure 4.13: *The resultant velocity 100 ms after the air injection*

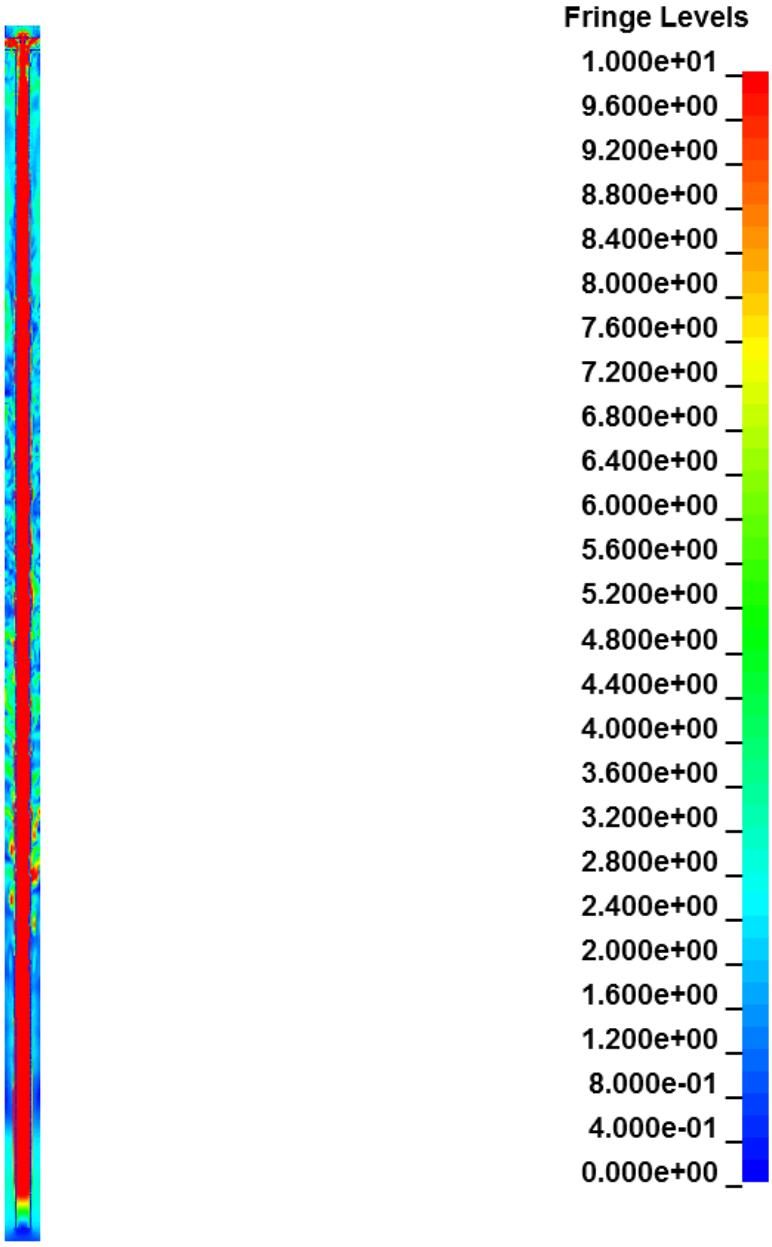

Figure 4.14: *The resultant velocity 206 ms after the air injection*

4.2.2 Bag dynamics

As a result of the initial flow, the bag had a deformation between the rods. Since the used solver was an explicit solver, no stationary initial deformation existed but instead the bag oscillated a bit but with a relatively small amplitude. The initial deformation at the top could be seen in Figure 4.15. The initial deformation in the bottom of the bag was much smaller than the top. When the cleaning process started the bag got expanded

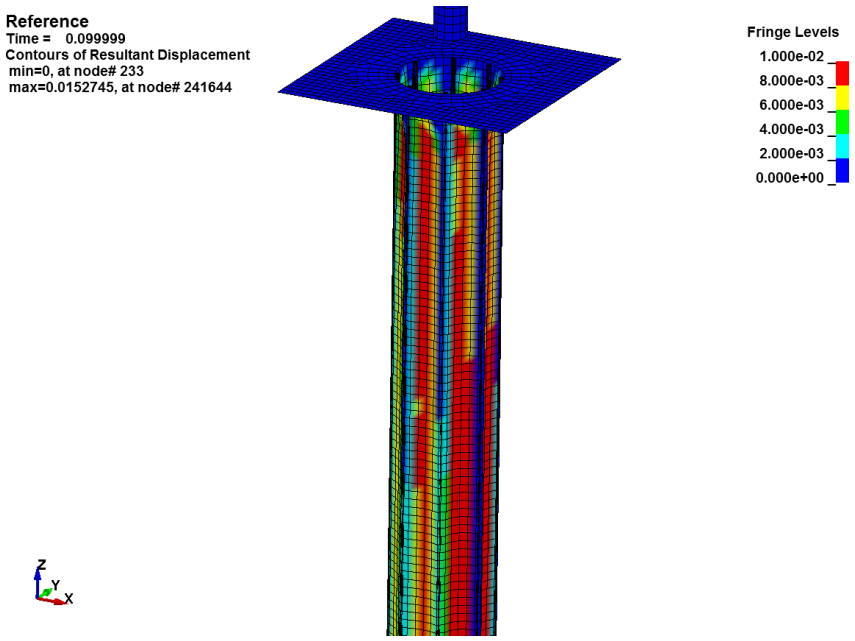

Figure 4.15: *The initial deformation at the top of the bag*

by the injected air. After the air passed a point on the bag, the bag started to oscillate at this point. The reason for that may be that when the high pressure air have passed, an area of lower pressure air passed by, as could be seen in Figure 4.10, which made the bag crumple. But when the bag hit the cage it started to bounce back which is the reason why the bag started to oscillate. The expansion of the bag due to the flow from the cleaning in a cut plane 1 m down the bag in lengthwise direction could be seen in Figure 4.16.

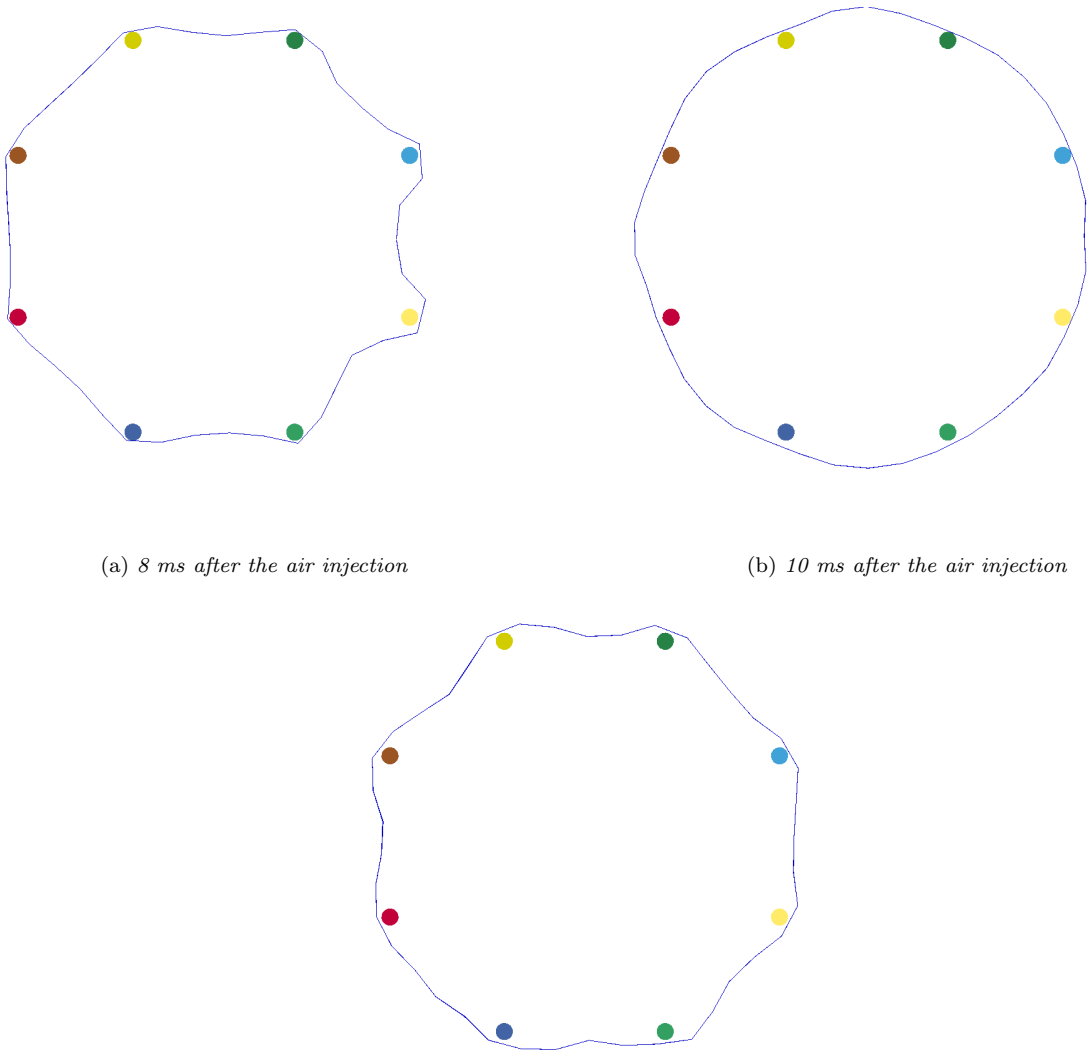

(a) *8 ms after the air injection*

(b) *10 ms after the air injection*

(c) *12 ms after the air injection*

Figure 4.16: *The expansion for the reference case*

Accelerations in the bag

Due to the interaction between with the injected air, the bag got an acceleration. The acceleration is important for the cleaning of the bag. When the bag starts to expand, both the bag and the dust increase its radial velocity. When the bag reaches its maximum expansion the radial velocity slows down rapidly and the dust fly of. The acceleration were measured in a point between two rods, in this case between the rods to the right in Figure 4.16. The acceleration as a function of time could be seen in Figure 4.17 and the radial displacement could be seen in Figure 4.18. In the figures some of the results were missing (long straight lines, except from the straight lines before 0.1 s where the sampling interval was much lower).

Here the maximum acceleration was $a_{\max} = 26 \cdot 10^3\,\mathrm{m/s^2}$ and the minimum was $a_{\min} = -15 \cdot 10^3\,\mathrm{m/s^2}$. The acceleration may not be correct due to the incorrect pressure pulse, but here these results was used to compare how the acceleration differed between different cases. During expansion, the maximum displacement in the bag was $-1 \cdot 10^{-3}\,\mathrm{m}$ which mean that the bag did not reach beyond its reference state (undeformed state). After a closer look it seemed that the lowest acceleration did not occur at the maximum displacement, which seemed strange. A close up of Figure 4.17 and 4.18 could be seen in Figure 4.19 and 4.20. Here it could be

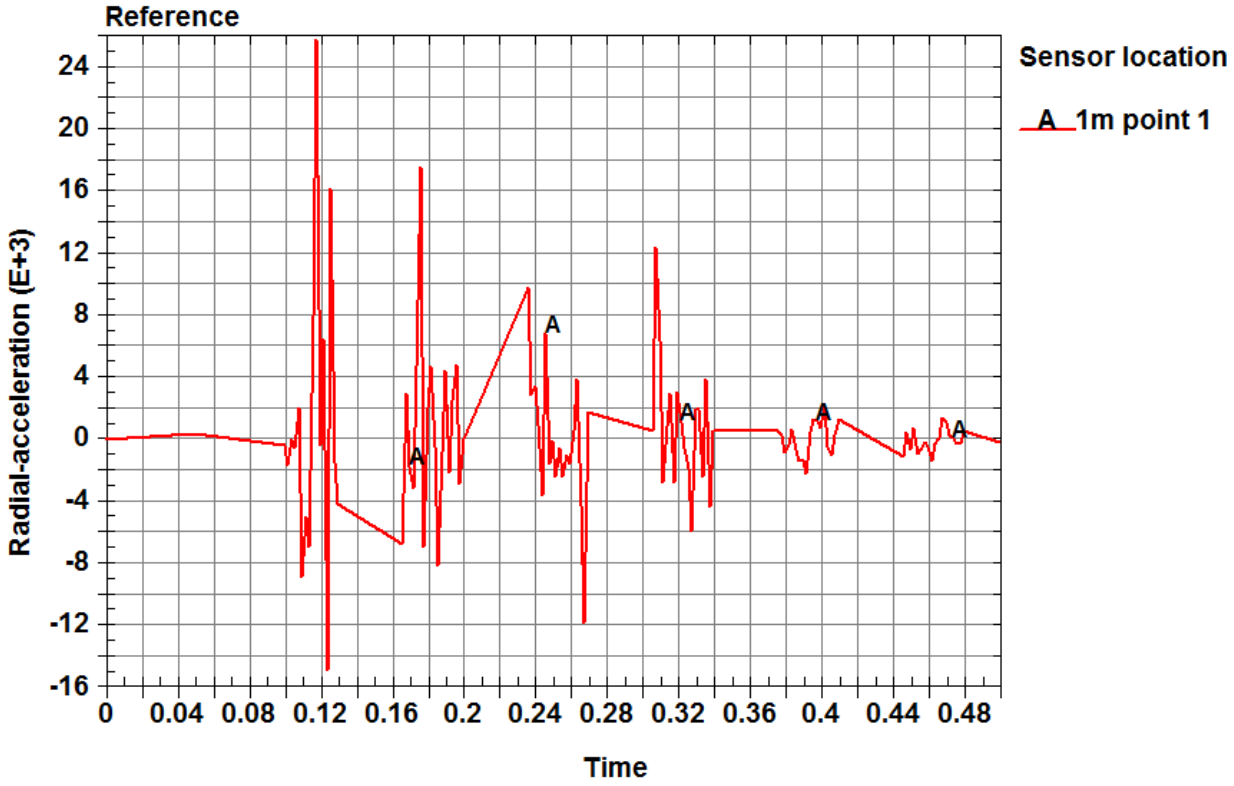

Figure 4.17: *The radial acceleration for a point located between two rods 1m downwards the bag*

seen that the maximum displacement occurred at time 0.110 s and the corresponding acceleration at this time was $-9 \cdot 10^3\,\mathrm{m/s^2}$. The reason for why the lowest acceleration did not occur at the location of the maximum displacement was not understood, not even after studying every sampled time step. In the rest of the thesis only the acceleration at the largest expansion and the acceleration when the bag bounce on the cage were considered. Due to that the result from this point was a bit strange, another point between the rods located at the top in e.g Figure 4.16 was considered. This point was called point 2 and the radial acceleration and radial displacement at this point could be seen in Figure 4.21 and 4.22. At this point the displacement at the expansion reached beyond the reference (undeformed) state. This might be a large reason why the lowest acceleration at this point actually occurred at the same time as the maximum displacement from the expansion. The maximum displacement at point 2 was $1.5 \cdot 10^{-3}\,\mathrm{m}$ and the resulting acceleration was $-33 \cdot 10^3\,\mathrm{m/s^2}$. As could be seen in Figure 4.22 the bag bounce on the cage which gave rise to the positive accelerations. In both points there was a positive acceleration in the size of $2 \cdot 10^3\,\mathrm{m/s^2}$ in the beginning of the expansion, approximately at time 0.108 s. This acceleration gave rise to the radial velocity and the differences after that may be due to differences in the initial deformation.

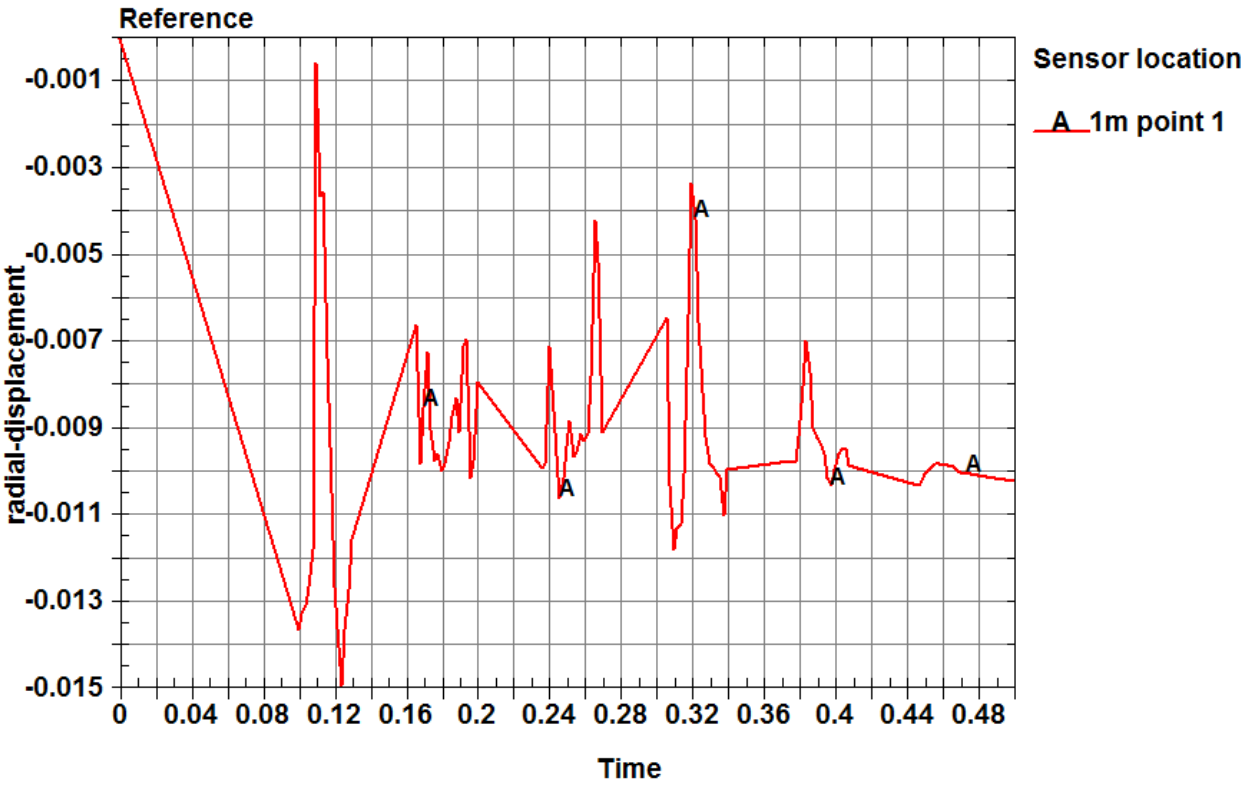

Figure 4.18: *The displacement of the bag at a point between two rods. The zero displacement state is the state where no initial flow deforms the bag.*

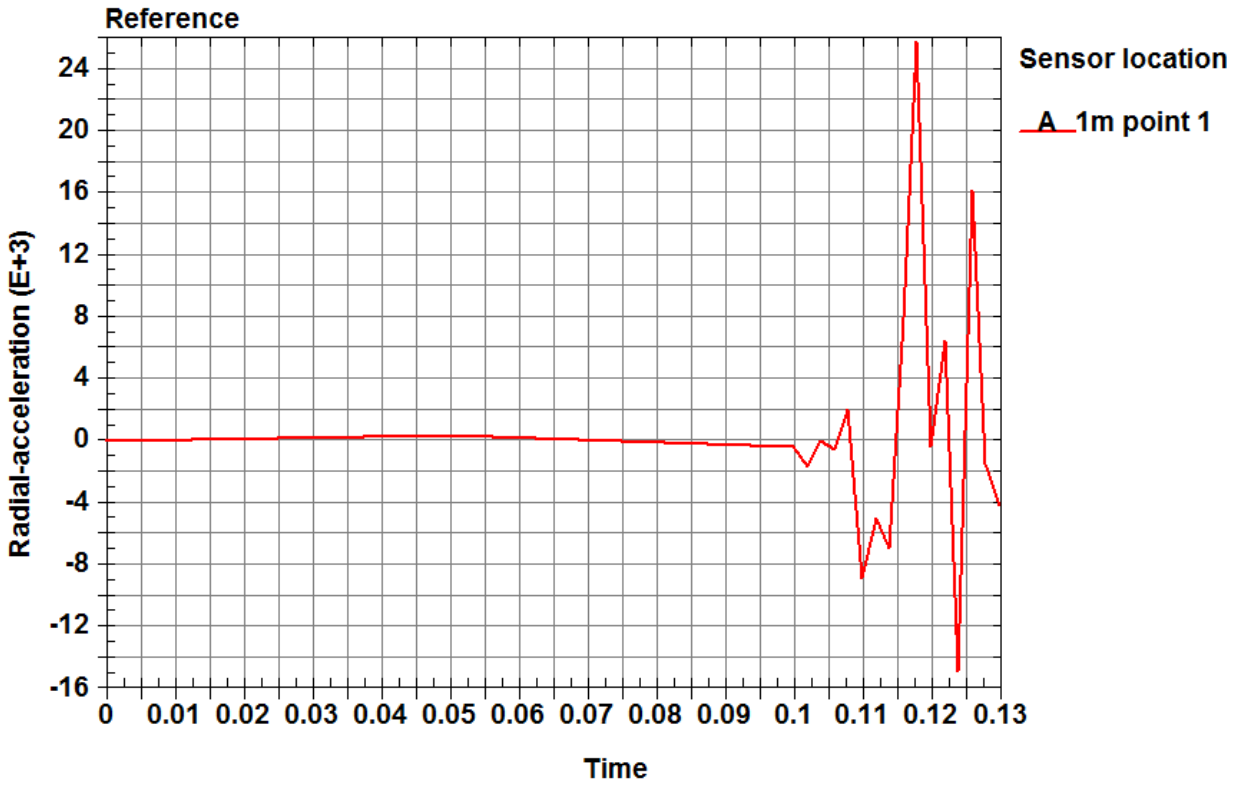

Figure 4.19: *A close up of the radial acceleration*

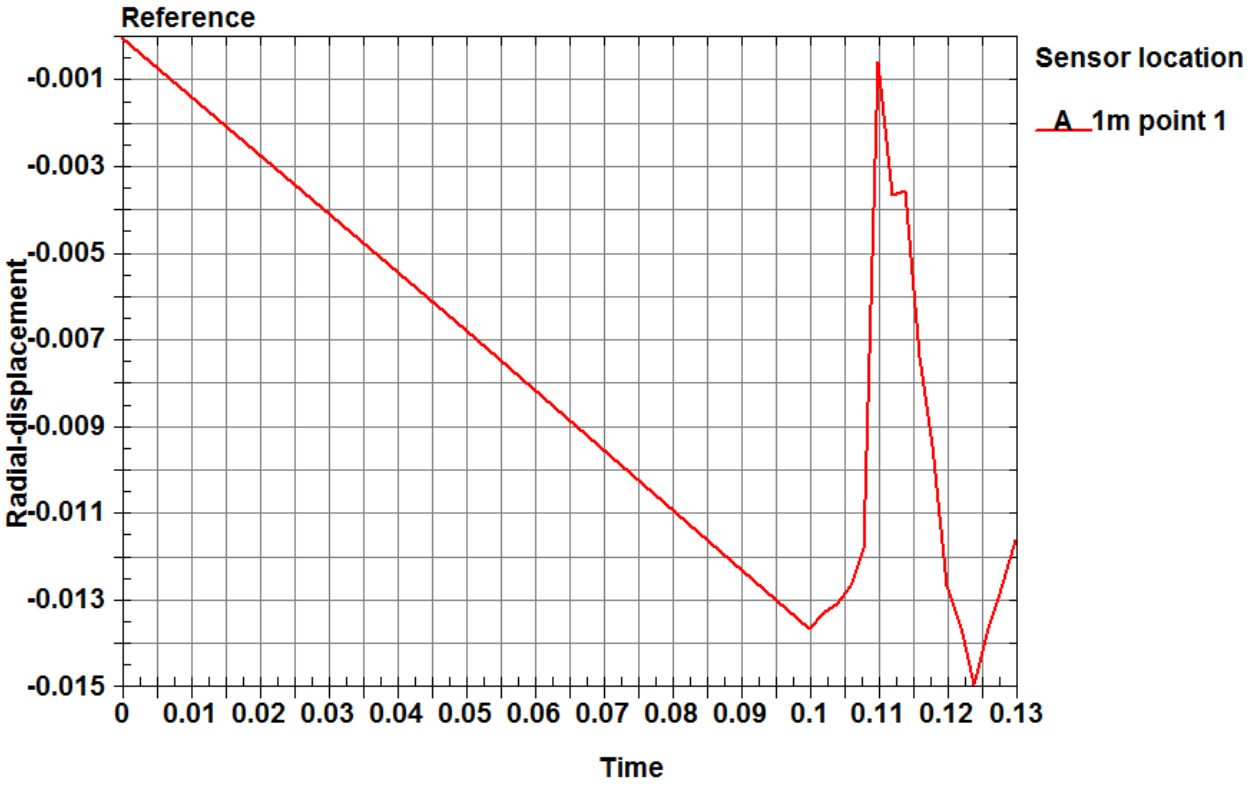

Figure 4.20: *A close up of the radial displacements*

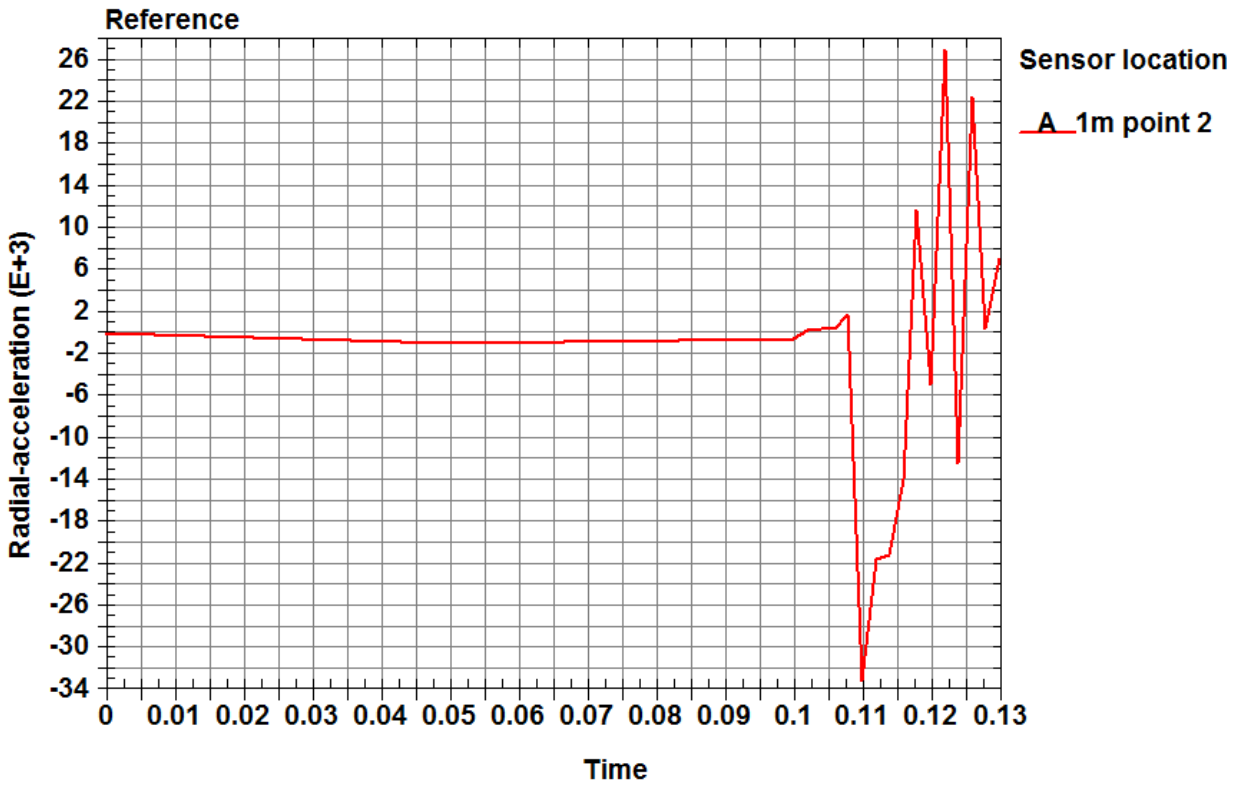

Figure 4.21: *The radial acceleration at point 2*

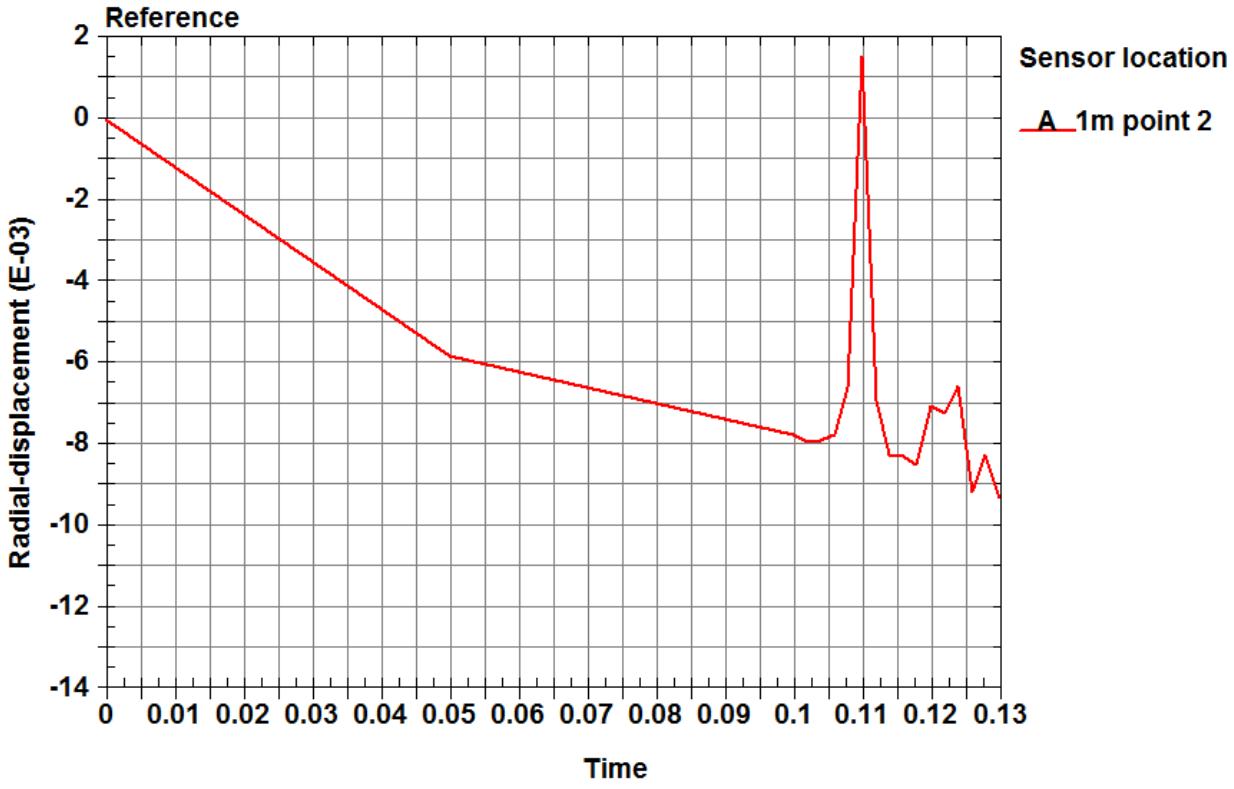

Figure 4.22: *The radial displacements at point 2*

4.3 Cases with different permeability

Lower permeability of the bag means that less air could flow through the bag at a specific pressure drop. This should increase the pressure at the bag surface due to the injected air still needs to get somewhere. The cases considering different permeability in this thesis was case 1 and case 2. The pressure increased to an amplitude of 2300 Pa for case 1 and to 2600 Pa for case 2. The pressure amplitude for the reference was 1850 Pa. The resulting accelerations for the different cases compared with the reference case could be seen in Table 4.1 for point 1 and in Table 4.2 for point 2. As could be seen in the tables the acceleration differed both between the

Table 4.1: The maximum and minimum accelerations, $a_{\min}$ and $a_{\max}$, at point 1 for the cases with different permeability

Case	$\boldsymbol{a}_{\min}$, [m/s^2]	$\boldsymbol{a}_{\max}$, [m/s^2]	**Radial displacement,** [m]
Reference	$-9 \cdot 10^3$	$26 \cdot 10^3$	$-1 \cdot 10^{-3}$
Case 1	$-39 \cdot 10^3$	$20 \cdot 10^3$	$3 \cdot 10^{-3}$
Case 2	$-33 \cdot 10^3$	$5 \cdot 10^3$	$5 \cdot 10^{-3}$

Table 4.2: The maximum and minimum accelerations, $a_{\min}$ and $a_{\max}$, at point 2 for the cases with different permeability

Case	$\boldsymbol{a}_{\min}$, [m/s^2]	$\boldsymbol{a}_{\max}$, [m/s^2]	**Radial displacement,** [m]
Reference	$-33 \cdot 10^3$	$26 \cdot 10^3$	$1.5 \cdot 10^{-3}$
Case 1	$-6 \cdot 10^3$	$6 \cdot 10^3$	$0.4 \cdot 10^{-3}$
Case 2	$-11 \cdot 10^3$	$9 \cdot 10^3$	$0.5 \cdot 10^{-3}$

cases and on which point that was considered. In point 1 the acceleration magnitudes was higher for case 1 and in point 2 it was the opposite. This was a bit unexpected since the pressure for case 2 was higher than the pressure for case 1 which should result in that case 2 should have had higher magnitudes of the accelerations. The reason for this was not clarified during this thesis.

4.4 Case with different dust cake weight

When dust got stuck on the bag surface the bag became heavier. If the acting force on the bag was the same, this would result in a lower acceleration according to Newton's second law, $F_i = ma_i$. In this thesis the case 3 and 4 considered the extra weight on the bag due to dust. Case 3 considered 1 kg/m^2 extra weight due to dust and case 4 considered 3 kg/m^2. The accelerations could be seen in Table 4.3. The accelerations were at a

Table 4.3: The maximum and minimum accelerations, $a_{\min}$ and $a_{\max}$, at point 1 for the cases with different dust cake weight

Case	$\boldsymbol{a}_{\min}$, [m/s^2]	$\boldsymbol{a}_{\max}$, [m/s^2]	**Radial displacement,** m
Reference	$-9 \cdot 10^3$	$26 \cdot 10^3$	$-1 \cdot 10^{-3}$
Case 3	$-65 \cdot 10^3$	$25 \cdot 10^3$	$7 \cdot 10^{-3}$
Case 4	$-9 \cdot 10^3$	$17 \cdot 10^3$	$0.5 \cdot 10^{-3}$

first sight a bit surprising. The magnitude of the negative acceleration increased a lot for case 3 but for case 4 the negative acceleration was the same as for the reference case. The maximum positive acceleration was approximately the same for case 3 and the reference case. For case 4 the acceleration was lower compared to the reference case. To understand this the expansion for both cases were studied and could be seen in Figure 4.23 and 4.24. The initial deformation, also called slack, was much larger for case 3 in the measured point (between the rods to the right). Due to the initial deformation in case 3 the bag could accelerate a longer distance which results in a higher radial velocity and thereby also larger radial deformation and higher magnitude on the negative acceleration. This initial deformation seems to have a large impact on the acceleration on the bag, and since the initial deformation, of some reason, was so different it was hard to compare the accelerations due to the dust cake weight. Therefore the accelerations was also measured in another point. From the figures

describing the expansion, a point located between the rods at the top was considered to have a similar initial deformation. The accelerations in that point could be seen in Table 4.4. These values were more as expected.

Table 4.4: The maximum and minimum accelerations, $a_{\min}$ and $a_{\max}$, at point 2 for the cases with different dust cake weight

Case	$\boldsymbol{a}_{\min}$, [m/s^2]	$\boldsymbol{a}_{\max}$, [m/s^2]	**Radial displacement,** [m]
Reference	$-33 \cdot 10^3$	$26 \cdot 10^3$	$1.5 \cdot 10^{-3}$
Case 3	$-5 \cdot 10^3$	$15 \cdot 10^3$	$0.5 \cdot 10^{-3}$
Case 4	$-1.5 \cdot 10^3$	$2.6 \cdot 10^3$	$0.25 \cdot 10^{-3}$

Case 4 which had the most dust accelerated slower than the other cases. But since it was such a big difference between the measured points it was hard to draw any conclusions without averaging the accelerations over the whole circumferential of the bag.

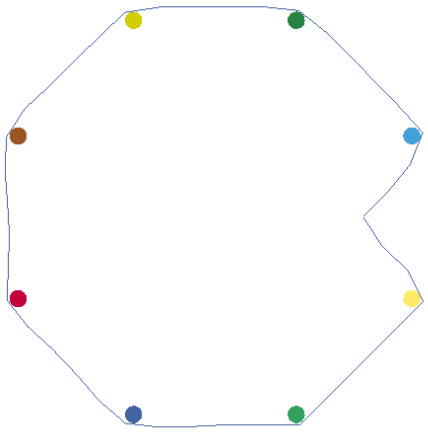

(a) *8 ms after the air injection*

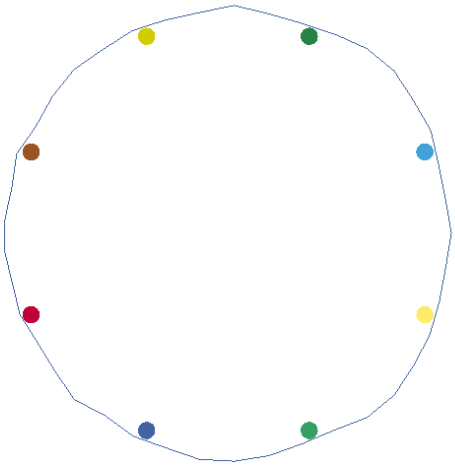

(b) *12 ms after the air injection*

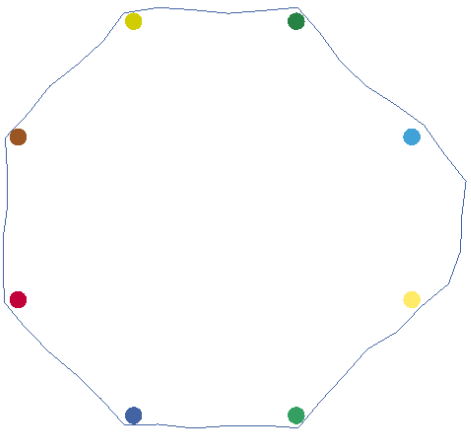

(c) *16 ms after the air injection*

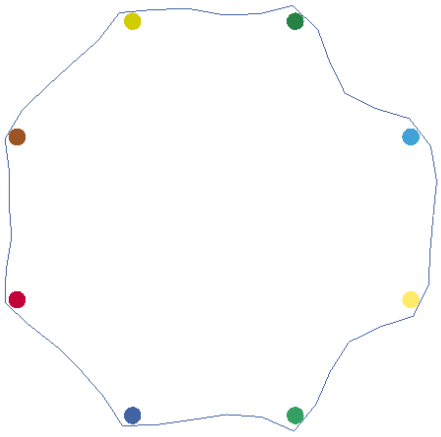

(d) *20 ms after the air injection*

Figure 4.23: *The expansion for case 3*

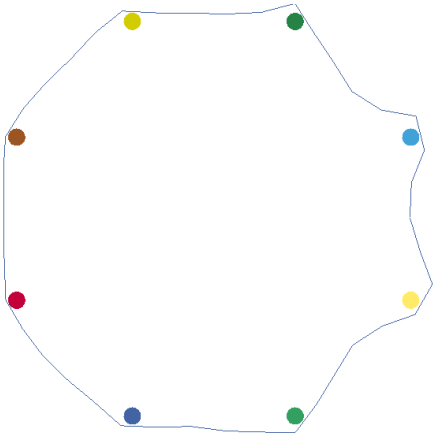

(a) *8 ms after the air injection*

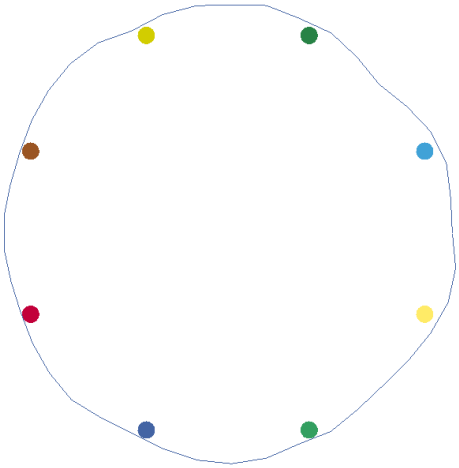

(b) *12 ms after the air injection*

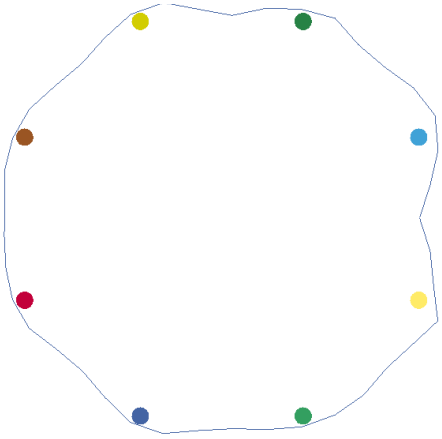

(c) *16 ms after the air injection*

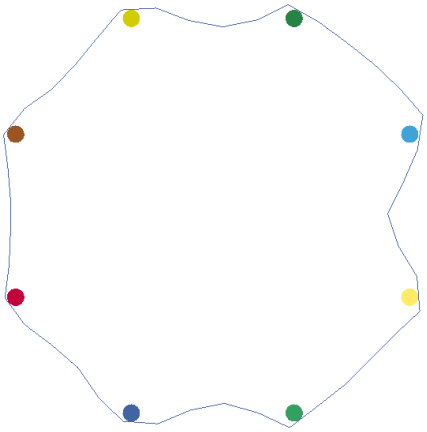

(d) *20 ms after the air injection*

Figure 4.24: *The expansion for case 4*

5 Discussion

The simulations made in this thesis failed to predict the pressure pulse during the injection. According to experiments, the pressure pulse should propagate significantly faster and with a higher magnitude than predicted from the simulations. The reason for this have probably something to do with the pressure boundary condition above the nozzle (the surface where the air injection occur). This boundary condition, describing the total pressure, have been tested in several ways. At first, the boundary condition was put at the nozzle inlet. But since the pressure pulse did not propagate correctly a new boundary condition was set on a larger surface. This was done because it was unsure how LS-DYNA defined the pressure at a segment, i.e if it was static or total pressure that was defined. The approach of defining the total pressure on a larger surface was made because of that the total pressure approximates the static pressure if the velocity is low. If the pressure boundary condition was put on a larger surface, the velocity at the boundary would be lower and therefore the effect of the dynamic pressure would decrease. Still, this was not enough to solve the problem with the pressure propagation. The next try was to pre-pressurize the air above the nozzle and prevent the air from flowing through the nozzle inlet until the cleaning process started. This was done with a wall boundary condition at the nozzle inlet and was suddenly deleted when the cleaning process started. Here the pressure propagated much faster. It actually propagated with the speed of sound, but unfortunately only for while and it also got some numerical issues and gave non-physical velocities through the bag. But from this simulation, it was shown that just the pressure boundary condition was not sufficient to trigger the pressure pulse propagation correctly. Due to time limitation, it was decided to continue with some parameter studies. But if there was more time, it would be a top priority to find a new way to model the injection. A way could be to model the full scale tank but today that would be too computational demanding.

The acceleration in the bag was expected to increase with lower permeability due to that the pressure should increase if less air was flowing through the bag surface (more air remains inside the bag). If dust got stuck on the bag surface it was expected that the bag would react slower on the changes in the flow field due to higher inertia and the acceleration magnitudes would decrease with the weight of the dust cake. But as could be seen in the result chapter, this was not the case. The trends were hard to predict and the expectations were only fulfilled at point 2 for the cases with different dust cake weight. The reason for the unexpected results was probably the uneven initial deformation (also called slack). The slack was much higher in one locations (point 1 for all cases). In some cases the slack resulted in that the expansion did not reach the undeformed state, but in case 3 this initial slack was much larger than the other cases and this resulted in that the bag could accelerate for a longer distance. This resulted in that the bag expanded a lot. Since it seems that the initial slack affects the accelerations a lot in the simulations, it could not be seen in the simulations how the studied parameters affected the bag. Since the simulations were transient, the initial deformation changed with time and therefore the accelerations may have looked different if the injection should have started in a different time. Why there was an uneven slack in the simulations was not understood. It was expected to be approximately the same slack between all the rods, but this was not the case in the simulations. In reality, the number of rods are higher and the initial slack should be smaller than in the simulations. Also, since the accelerations differed a lot in different points in the same case, some kind of standard should be implemented about how the accelerations should be measured.

The initial deformation were much larger at the top compared to the bottom of the bag. In the simulations this was because the pressure difference between the inside and the outside of the bag was much larger at the top than the bottom due to the lower pressure above the bag plate. This resulted in that the most of the air flowed through the bag at the top and almost nothing in the bottom. This may not be the case in reality and the problem was probably because two pressure boundary conditions were used (i.e the pressure gradient, $\partial p/\partial x_i$, which drives the flow was larger at the top than the bottom). Maybe a velocity boundary condition at the boundaries at the air part below the bag plate could have been a better choice. This velocity could be estimated if the amount of air flowing into the fabric filter was known. Also the initial flow was only running for 0.1 s. Even if it seemed to be steady at a first sight, maybe a longer initial solution could affect the deformations in the lower parts of the bag. But running the initial solution for a longer time is expensive. Due to that LS-DYNA used an explicit solver, the time step needed to be small enough to be conditionally stable. In the simulations in this thesis the stable time step was between $1 - 5 \cdot 10^{-6}$ s and this resulted in many time steps. The simulation of the reference case, which was simulated for 0.5 s, took 5-6 days on 16 cores. The other simulations were shorter but still took approximately 2 days on 16 cores. Also [7] states that the compressible ALE solver in LS-DYNA was developed for short duration problems with high pressure and velocity gradients

and therefore does not suit well for flows with low pressure gradients.

5.1 Future work

This thesis was a first step of modelling the dynamics of a bag during cleaning. To be able to use this kind of simulations to improve the cleaning process, the model needs to be modified. A list of things that needs to be done follows:

- The pressure pulse and injection of air needs to be modelled in such a way that the pressure propagates faster and with the right pressure magnitude. The amount of injected air should be approximately the same as in this thesis.
- The initial deformation may need to be distributed in a more even way
- The dynamics of the bag should be investigated in the bottom of the bag to see if the lower parts of the bag get cleaned
- Also simulations of longer bags could be interesting, because longer bags could filter more air
- Fabric material often have anisotropic or orthotropic material behaviours and this could be included in a future project
- The parameter studies could include more simulations on every case and also include other parameters like different Young's modulus, different size of the pressure pulse from the cleaning, different initial flow, different distribution of the dust on the bag etc

6 Conclusions

The aim of this thesis was to evaluate the dynamics of a bag when a pressure pulse was injected inside a deformable porous fabric bag. The simulations did not agree to experimental values but still it is too early to reject the modelling approach. If the injected air is modelled with another boundary condition it might be possible to study the dynamics of the bag. This thesis shows that it might be possible to model the cleaning of the bag. The model included the fluid structure interaction between flowing air and a porous fabric. Also a contact between the bag and the cage was included to prevent the bag from to large deformation (crumpling). All this was included in the Arbitrary Lagrangian-Eulerian method. A great advantage of using the ALE method is the fact that it is only one code, which means that it does not have to communicate with other programs.

The dynamics of the bag showed different results in different points and a need of a standard of how these result should be measured needs to be defined if the results should make any sense. Also, since the solver was an explicit solver there did not exist a steady initial solution. Therefore the initial solution differed at different times and with different cases. The uneven slack in the simulations affected the bag in a way that was not understood at the time of this thesis. To be able to analyse the dynamics of the bag, the initial slack should be controlled somehow so it does not affect the solution to much.

Since the model predicted the pressure pulse was not accurate in all respects, also the accelerations were not accurate. But with improvement of the boundary condition, the modelling approach may be sufficient.

References

[1] ALSTOM. *Air Quality Control Systems. Pure Air, Clean Solutions.* Online; accessed 11-February-2014. URL: http://www.alstom.com/Global/Power/Resources/Documents/Brochures/air-quality-control-systems.pdf.

[2] ALSTOM. *NID Flue Gas Desulphurization.* Online; accessed 11-February-2014. URL: http://www.alstom.com/Global/Power/Resources/Documents/Brochures/nid-flue-gas-desulphurisation.pdf.

[3] J. D. Anderson. *Modern Compressible Flow. with historical perspective.* 3rd ed. McGraw-Hill, 2004. ISBN: 007-124136-1.

[4] N. Aquelet. ALE Adaptive Mesh Refinement in LS-DYNA. *12th International LS-DYNA Users Conference* (2012).

[5] A. Boström. *Rigid Body Dynamics.* Oct. 2013.

[6] L. Davidsson. *Fluid mechanics, turbulent flow and turbulence modeling.* Sept. 2012.

[7] J. Day. *Guidelines for ALE modelling in LS-DYNA.* Oct. 2010.

[8] A. Derviux et al. Total energy conservation in ALE schemes for compressible flows. *European Journal of Computational Mechanics* (2010).

[9] J Donea et al. "Arbitrary Lagrangian-Eulerian Methods". *Encyclopedia of Computational Mechanics. Fundamentals.* Vol. 1. John Wiley & Sons Ltd, 2004. ISBN: 0-470-84699-2.

[10] M. Ekh. *TME075 Mechanics of solids - linear elasticity.* Sept. 2012.

[11] Environmental Protection Agancy - United States. *Human Health and Environmental Effects of Emissions from Power Generation.* Online; accessed 11-February-2014. URL: http://www.epa.gov/captrade/documents/power.pdf.

[12] N. Erzaz Shahabi, S. Saharkhiz, and S Mohmammad Hosseini Varkiyani. Effect of Fabric Structure and Weft Density on the Poission's Rato of Worsted Fabric. *Journal of Engineering Fibers and Fabrics* (2013).

[13] M. Forsblom. "Supersonic Artillery Projectile Fin Deployment Simulation Methodology". MA thesis. Luleå University of Technology, June 2013.

[14] Franhofer Institute for High-Speed Dynamics, Ernst-Mach-Institute. *Characterization and Modeling of Fabric Materials.* Online; accessed 21-April-2014. URL: http://www.en.emi.fraunhofer.de/business-segments/transport/characterization-and-modeling-of-fabric-materials/.

[15] A. Haufe, K. Weimar, and U. Göhner. *Advanced Airbagsimulation using Fluid-Structure-Interaction and the Eulerian Method in LS-DYNA.* 2004.

[16] Livermore Software Technology Corporation. *LS DYNA - Keyword User's Manual. Volume 1.* 2014.

[17] Livermore Software Technology Corporation. *LS DYNA - Keyword User's Manual. Volume 2.* 2014.

[18] Livermore Software Technology Corporation. *LS-DYNA - Theory Manual.* 2014.

[19] L. Olovsson. *Training class in ALE and fluid-structure interaction.* 2006.

[20] N. Ottosen and H. Petersson. *Introduction to the Finite Element Method.* Pearson, 1992. ISBN: 978-0-13-473877-2.

[21] SIMULIA. *Abaqus Analysis User's Manual.* Version 6.12.

[22] SIMULIA. *Simulation of Airbag Deployment Using Coupled Eulerian-Lagrangian Method in Abaqus/Explicit.* June 2011.

[23] B. Sundström, ed. *Handbok och formelsamling i Hållfasthetslära.* Instutionen för hållfasthetslära KTH, 1999.

[24] B. Tutt et al. Finite Mass Simulation Techniques in LS-DYNA. *21st AIAA Aerodynamic Decelerator Systems Technology Conference and Seminar* (2011).

[25] B. Tutt. The Application of a New Material Porosity Algorithm for Parachute Analysis. *9th International LS-DYNA Users Conference* (2006).

[26] B. Tutt et al. Development of Parachute Simulation Techniques in LS-DYNA. *11th International LS-DYNA Users Conference* (2010).

[27] J. Wang et al. Porous Euler-Lagrange Coupling: Application to Parachute Dynamics. *9th International LS-DYNA Users Conference* (2006).

[28] Wikipedia. *Cauchy Stress Tensor — Wikipedia, The Free Encyclopedia.* [Online; accessed 6-April-2014]. 2013. URL: http://en.wikipedia.org/wiki/Cauchy_stress_tensor.

[29] G. Xing-long et al. Fluid-Structure Interaction Simulation of Parachute in Low Speed Airdrop. *Proceedings of the World Congress on Engineering* **3** (July 2013).

[30] R. Zong. “Finite Element Analysis of ship-ice collision using LS-DYNA”. MA thesis. Memorial University of Newfoundland, July 2012.

A Index notation and Einstein convention

Index notation is a way to express vectors and tensors. As an example of the usage of index notation, see the vector $\mathbf{a}$ defined by the tensor $\mathbf{T}$ and the vector $\mathbf{b}$ in eq (A.1)

$$\mathbf{a} = \mathbf{T}\mathbf{b} \tag{A.1}$$

The vectors and tensor in eq (A.1) are expressed as

$$\mathbf{a} = \begin{bmatrix} a_1 \\ a_2 \\ a_3 \end{bmatrix}; \quad \mathbf{T} = \begin{bmatrix} T_{11} & T_{12} & T_{13} \\ T_{21} & T_{22} & T_{23} \\ T_{31} & T_{32} & T_{33} \end{bmatrix}; \quad \mathbf{b} = \begin{bmatrix} b_1 \\ b_2 \\ b_3 \end{bmatrix} \tag{A.2}$$

The components in $\mathbf{a}$ can be written explicitly

$$\begin{aligned} a_1 &= T_{11}b_1 + T_{12}b_2 + T_{13}b_3 \\ a_2 &= T_{21}b_1 + T_{22}b_2 + T_{23}b_3 \\ a_3 &= T_{31}b_1 + T_{32}b_2 + T_{33}b_3 \end{aligned} \tag{A.3}$$

and in a more general way (A.3) looks like

$$a_i = \sum_{j=1}^{3} T_{ij}b_j \tag{A.4}$$

where i is called free index since it only appear once in each term. This equation can be written with Einstein convention where an index is summarized if it appear twice in a term. An index that is summarized is called dummy index and using Einstein convention eq (A.4) with dummy index j is written as

$$a_i = T_{ij}b_j \tag{A.5}$$

It is easy to express scalar and vector products with index notation and Einstein convention. Assume that we have two vectors $\mathbf{c}$ and $\mathbf{d}$ expressed in a coordinate system with orthonormal basis vectors $\hat{\mathbf{e}} = (\hat{e}_1, \hat{e}_2, \hat{e}_3)$

$$\begin{aligned} \mathbf{c} &= c_i\hat{e}_i = c_1\hat{e}_1 + c_2\hat{e}_2 + c_3\hat{e}_3 \\ \mathbf{d} &= d_j\hat{e}_j = d_1\hat{e}_1 + d_2\hat{e}_2 + d_3\hat{e}_3 \end{aligned} \tag{A.6}$$

In eq (A.6) c_i and d_j are scalar components. The scalar product of $\mathbf{c}$ and $\mathbf{d}$ is defined as

$$\mathbf{c} \cdot \mathbf{d} = c_i\hat{e}_i \cdot d_j\hat{e}_j = c_i d_j \hat{e}_i \cdot \hat{e}_j \tag{A.7}$$

Since $\hat{e}_i$ and $\hat{e}_j$ in eq (A.7) are orthonormal basis vectors it means that the scalar product equals zero if they are two different basis vectors. That means that eq (A.7) now can be written as

$$\mathbf{c} \cdot \mathbf{d} = c_i d_j \hat{e}_i \cdot \hat{e}_j = c_i d_j \delta_{ij} = c_i d_i \tag{A.8}$$

where δ_{ij} is the Kronecker's delta

$$\delta_{ij} = \begin{cases} 1 & \text{If} \quad i = j \\ 0 & \text{If} \quad i \neq j \end{cases} \tag{A.9}$$

The vector product of $\mathbf{c}$ and $\mathbf{d}$ can be written as in eq (A.10)

$$\mathbf{c} \times \mathbf{d} = c_i d_j \hat{e}_i \times \hat{e}_j = c_i d_j \epsilon_{ijk} \hat{e}_k \tag{A.10}$$

Since a vector product of two equal vectors is zero, only different values of i, j, k will contribute with non-zero values to the vector product. The sign of the vector product follows the right hand rule and therefore the permutation symbol, ϵ_{ijk}, is defined as

$$\epsilon_{ijk} = \begin{cases} 1 & \text{If } ijk = 123,\ 231,\ 312 \\ -1 & \text{If } ijk = 321,\ 213,\ 132 \\ 0 & \text{Else} \end{cases} \tag{A.11}$$

B Proof of symmetric stress tensor

For a continuum body the moment, M_i, around an arbitrary point equals the rate of the linear momentum $\dot{L}_i$.

$$M_i = \dot{L}_i \quad \text{where} \quad L_i = I_{ij}\omega_j \tag{B.1}$$

In eq (B.1) I_{ij} is the moment of inertia of the body and ω_j is the angular velocity. If the body is in equilibrium the angular velocity ω_j is constant which reduce eq (B.1) to

$$M_i = 0 \tag{B.2}$$

Consider the body in Figure B.1, which is in equilibrium. The moment around the origin, O, is defined as

$$M_{i,O} = \int_S \epsilon_{ijk} x_j T_k^{(n)} \mathrm{d}S + \int_V \epsilon_{ijk} x_j F_k \mathrm{d}V \tag{B.3}$$

where x_j is the distance from the point O ($\mathbf{r} = x_j \hat{e}_j$ in the figure where $\hat{e}_j$ denote the basis vectors), $T_k^{(n)}$ is the surface traction per unit area, S is the surface of the body, F_k is the body forces per unit volume and V is the volume of the body. The surface traction is the stresses in the normal direction which means that it can be related to the stress tensor as

$$T_k^{(n)} = \sigma_{mk} n_m \tag{B.4}$$

where σ_{mk} is the stress tensor of the body and n_m is the normal. It is convenient to express the integrals

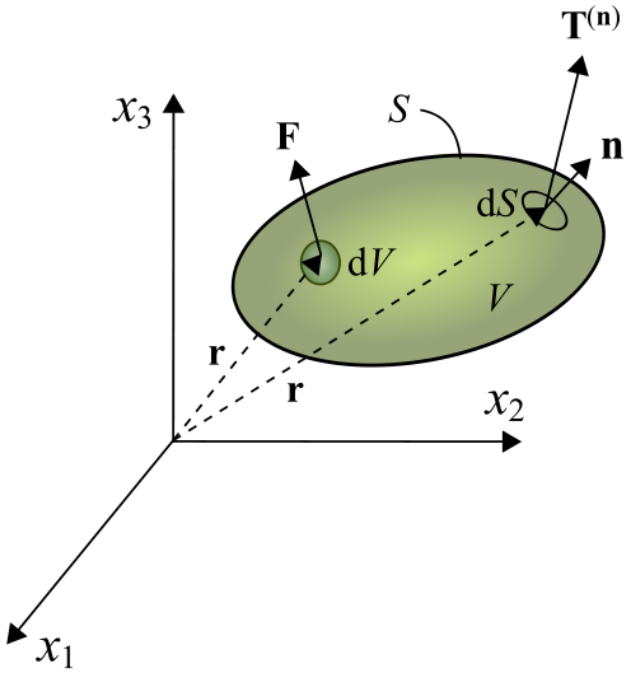

Figure B.1: *A body in equilibrium [28]*

in eq (B.3) in the same domain, either as surface integrals or volume integrals. For this purpose the Gauss' divergence theorem can be used. For an arbitrary tensor field variable B_{ij} the divergence of B_{ij} in a volume integral equals the surface traction of B_{ij} in the surface integral:

$$\int_V \frac{\partial B_{ij}}{\partial x_i} \mathrm{d}V = \int_S B_{ij} n_i \mathrm{d}S \tag{B.5}$$

Using eq (B.4), (B.5) and (B.3) in eq (B.2) gives the following equation:

$$\begin{aligned} 0 &= \int_S (\epsilon_{ijk} x_j \sigma_{mk}) n_m \mathrm{d}S + \int_V \epsilon_{ijk} x_j F_k \mathrm{d}V = \int_V \frac{\partial (\epsilon_{ijk} x_j \sigma_{mk})}{\partial x_m} \mathrm{d}V + \int_V \epsilon_{ijk} x_j F_k \mathrm{d}V \\ &= \int_V \epsilon_{ijk} \left(\frac{\partial x_j}{\partial x_m} \sigma_{mk} + x_j \left(\frac{\partial \sigma_{mk}}{\partial x_m} + F_k \right) \right) \mathrm{d}V \end{aligned} \tag{B.6}$$

Here the second term in the final expression contains the governing equation for conservation of momentum, which equals zero at equilibrium conditions. Also it should be noted that the partial derivative in the first term equals zero if $j \neq m$ and equals unity if $j = m$. Therefore this term equals the Kronecker's delta, δ_{jm}. The only non-zero terms appears when $j = m$ and eq (B.6) is now written as:

$$0 = \int_V \epsilon_{ijk}\sigma_{jk}\mathrm{d}V \tag{B.7}$$

The equation is valid for an arbitrary volume V which means that

$$\epsilon_{ijk}\sigma_{jk} = 0 \tag{B.8}$$

must be fulfilled. Doing the summation gives three relations

$$\epsilon_{123}\sigma_{23} + \epsilon_{132}\sigma_{32} = \sigma_{23} - \sigma_{32} = 0 \tag{B.9}$$

$$\epsilon_{213}\sigma_{13} + \epsilon_{231}\sigma_{31} = \sigma_{13} - \sigma_{31} = 0 \tag{B.10}$$

$$\epsilon_{312}\sigma_{12} + \epsilon_{321}\sigma_{21} = \sigma_{12} - \sigma_{21} = 0 \tag{B.11}$$

This can generally be written as

$$\sigma_{ij} = \sigma_{ji} \tag{B.12}$$

which proofs that the stress tensor, σ_{ij} is symmetric.

C Keyword input commands

Here the input file have been reduced to only show the commandos used in simulations.

*KEYWORD MEMORY
*TITLE
*CONTROL_ALE
*CONTROL_ENERGY
*CONTROL_MPP_DECOMPOSITION_DISTRIBUTE_ALE_ELEMENTS
*CONTROL_TERMINATION
*CONTROL_TIMESTEP
*DATABASE_GLSTAT
*DATABASE_GLSTAT_MASS_PROPERTIES
*DATABASE_MATSUM
*DATABASE_BINARY_D3PLOT
*DATABASE_FSI
*DATABASE_FSI_SENSOR
*BOUNDARY_NON_REFLECTING
*BOUNDARY_SPC_SET_ID
*SET_NODE_LIST
*BOUNDARY_SPC_SET
*LOAD_SEGMENT_SET
*CONTACT_ONE_WAY_SURFACE_TO_SURFACE
*SET_PART_LIST
*CONTACT_ONE_WAY_SURFACE_TO_SURFACE
*PART
*SECTION_SOLID
*MAT_RIGID
*SECTION_SHELL
*MAT_FABRIC
*MAT_NULL
*EOS_IDEAL_GAS
*DEFINE_CURVE
*SET_SEGMENT
*ALE_ESSENTIAL_BOUNDARY
*ALE_MULTI-MATERIAL_GROUP
*CONSTRAINED_LAGRANGE_IN_SOLID
*ELEMENT_SOLID
*ELEMENT_SHELL
*NODE
*END